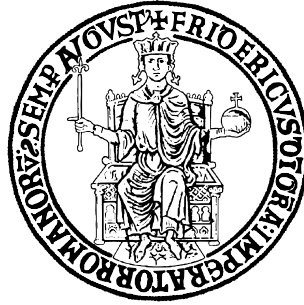


Università degli Studi di Napoli Federico II

DIPARTIMENTO DI INGEGNERIA INDUSTRIALE
SCUOLA POLITECNICA E DELLE SCIENZE DI BASE

TESI DI LAUREA MAGISTRALE IN INGEGNERIA AEROSPAZIALE



An Aerodynamic Assessment of the Hypersonic Aircraft STRATOFly using an Advanced Potential Method

Relatore:

Ch.mo Prof. Carlo de Nicola

Correlatori:

Dott. Paolo Caccavale - iBMB

Dott. Pietro Roncioni - CIRA

Dott. Antonio Schettino - CIRA

Candidato:

Francesco Gigante

MATRICOLA M53000962

Anno Accademico 2020-2021

*...a mia Mamma,
alla sua forza...*



Contents

1	PaMS code and Panel Methods	1
1.1	Mathematical formulation	1
1.2	Numerical procedure	7
1.2.1	Unsteady flows case	12
1.2.2	Velocity and forces computation	16
2	Test Case	19
2.1	Subsonic Diffuser	19
2.2	Delta Wing	23
3	The Hypersonic Aircraft STRATOFLY	29
3.1	About STRATOFLY	29
3.1.1	Geometry	31
3.2	CFD - CIRA	33
3.3	PaMS (Panel Method Solver)	35
3.3.1	Meshing	36
3.3.2	Setup	37
3.3.3	Internal and External Flow	38
3.3.4	External Flow	38
3.4	Results	41

Conclusions	51
Bibliography	53

Abstract

Under the frame of the European project STRATOFly, the present work was conducted together with CIRA (*Centro Italiano Ricerche Aerospaziali*) which main role is related to the aerodynamic analysis of the configuration case of study. According to CIRA research requirements, the objective was to study STRATOFly MR3 vehicle in the range of subsonic Mach numbers, in particular from $M=0$ to $M=0.7$, using an extremely quicker approach, with respect to the CFD, based on a modified low speed panel method.

Due to the extremely challenging design of the vehicle (Thin Lifting Surfaces, Body Flow, Duct), several preliminary test cases, including Euler CFD calculations, were performed in order to attest the panel method capability. The method PaMS (Panel Method Solver) was therefore selected to deal with the geometry uniqueness.

STRATOFly was analyzed using PaMS at $M = 0$ in the range of angles of attack from -6° up to 6° . Since the panel method is not able to capture the vortex force contribution by itself, Polhamus analogy was also applied together with a sensitivity study in relation to the leading edge surface considered. It was consequently possible to evaluate the lift, induced drag and pitching moment coefficients and compare them to CIRA Euler CFD results.

Chapter 1

PaMS code and Panel Methods

When dealing with a problem based on the equation of Laplace, there are different mathematical and numerical techniques which allow us to solve it, together with its boundary conditions. Panel methods (more specifically Boundary Element Methods) are based on Green's identities, implemented numerically by dividing the geometries in simple geometric elements (panels). In this chapter the main characteristics of these methods are explained, with a particular focus on PaMS code (Panel Method Solver), the method selected for STRATOFly MR3 assessment.

1.1 Mathematical formulation

Consider the scalar potential of velocity governed by Laplace equation

$$\nabla^2 \phi = 0 \tag{1.1}$$

The mathematical problem is described schematically in figure 1.1. An arbitrary body with boundary S_B is enclosed in a volume V , with outer boundary S_∞ . The boundary conditions are applied on this surfaces and the normal is

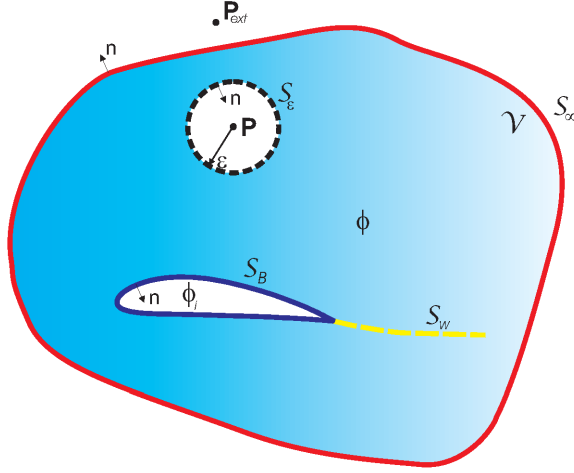


Figure 1.1: Fluid domain for potential flow

pointing to the outside of the region of interest V . It has been also defined the surface S_w representative of the wake and it is assumed to be infinitely thin.

Through the use of Green's identities it is possible to relate the solution of Laplace problem inside the volume V to the conditions imposed on the domain boundaries. Introducing the scalar potential $\frac{1}{r}$, where r is the generic distance from a point $P(x, y, z)$, and the potential of velocity ϕ both harmonic in V it is possible to define the Second Green's Identity

$$\int_S \left(\frac{1}{r} \nabla \phi - \phi \nabla \frac{1}{r} \right) \cdot \underline{n} dS = 0 \quad (1.2)$$

and the Third Identity

$$\phi(P) = \frac{1}{4\pi} \int_S \left(\frac{1}{r} \nabla \phi - \phi \nabla \frac{1}{r} \right) \cdot \underline{n} dS \quad (1.3)$$

Supposing that we are interested in the flow that occurs inside the S_B boundary, we can define the *internal potential* ϕ_i and in this case the point

P results to be outside of S_B . We can therefore apply the (1.2), resulting

$$0 = \int_S \left(\frac{1}{r} \underline{\nabla} \phi_i - \phi_i \underline{\nabla} \frac{1}{r} \right) \cdot \underline{n} dS \quad (1.4)$$

where \underline{n} points out of S_B . By adding equations (1.3) and (1.4) we obtain an expression similar to the Third Green's Identity that includes the influence of the internal potential.

$$\begin{aligned} \phi(P) = \frac{1}{4\pi} \int_{S_B} \left[\frac{1}{r} \underline{\nabla}(\phi - \phi_i) - (\phi - \phi_i) \underline{\nabla} \frac{1}{r} \right] \cdot \underline{n} dS + \\ + \frac{1}{4\pi} \int_{S_w + S_\infty} \left(\frac{1}{r} \underline{\nabla} \phi - \phi \underline{\nabla} \frac{1}{r} \right) \cdot \underline{n} dS \end{aligned} \quad (1.5)$$

The contribution of the S_∞ integral can be defined as

$$\phi_\infty(P) = \frac{1}{4\pi} \int_{S_\infty} \left(\frac{1}{r} \underline{\nabla} \phi - \phi \underline{\nabla} \frac{1}{r} \right) \cdot \underline{n} dS \quad (1.6)$$

This contribution depends on the reference frame and can be considered as a constant in an inertial system where the body moves in an uniform stream. Furthermore, since the wake surface S_w is assumed to be thin, $\partial\phi/\partial n$ results to be continuous across it. Therefore the equation (1.5) becomes

$$\begin{aligned} \phi(P) = \phi_\infty(P) + \frac{1}{4\pi} \int_{S_B} \left[\frac{1}{r} \underline{\nabla}(\phi - \phi_i) - (\phi - \phi_i) \underline{\nabla} \frac{1}{r} \right] \cdot \underline{n} dS + \\ + \frac{1}{4\pi} \int_{S_w} (\phi_U - \phi_L) \underline{\nabla} \frac{1}{r} \cdot \underline{n} dS \end{aligned} \quad (1.7)$$

which gives the value of the potential of velocity $\phi(P)$ in terms of the value of ϕ and $\partial\phi/\partial n$ on the boundary, that become the quantities needed to solve the problem together with the boundary conditions. In particular, since we are in a potential flow, the Neumann condition needs to be satisfied on the surface S_B , for which

$$\underline{n} \cdot \underline{\nabla} \phi = -V_{nT} - V_{nR} \quad (1.8)$$

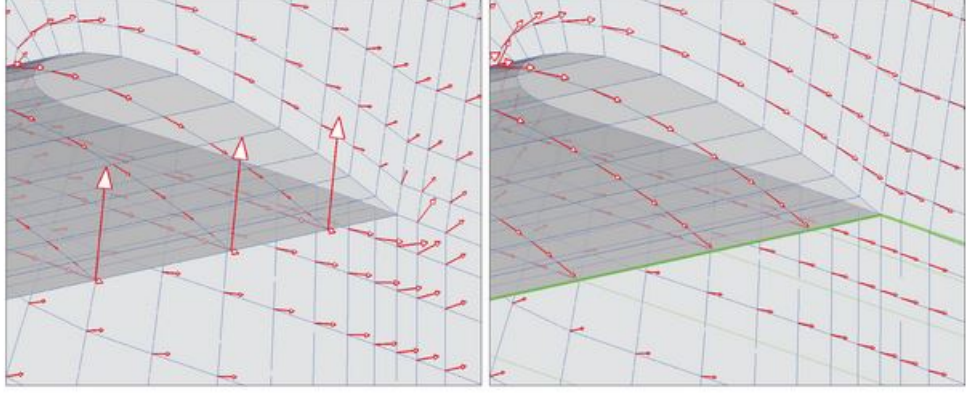


Figure 1.2: Flow field at the wing trailing edge without (left) and with (right) the imposition of the Kutta condition

where V_{nR} is the resultant of the normal component of the relative velocity between the fluid and the surface due to the motion of the body and/or to the asymptotic stream, while V_{nT} is the component related to an eventual flow of transpiration. No condition in terms of potential needs to be applied on the wake surface S_w , since its existence represents the imposition of Kutta condition at the trailing edge of three-dimensional aerodynamic bodies. The potential jump present in this integral must assure that the velocity does not rotate at the trailing edge, leaving the body along the direction imposed by the wake itself, as shown in figure 1.2. In this way the terms related to S_w are known, since the potential jump in the wake is directly related to the unknown potential at the trailing edge. A constraint is anyway necessary for the determination of the wake shape. Since it is not a solid surface, it cannot support any load. Therefore the wake shape must be aligned with the local flow direction, which in mathematical terms means that a tangency of velocity needs to be imposed in every point

$$\underline{V} \cdot \underline{n}|_{S_w} = 0 \quad (1.9)$$

properly orienting the local normal direction (flexible wake). Since the flow field \underline{V} is the unknown of our study, it is possible to solve the problem by approximating the wake with a predefined shape (rigid wake), unrelated to the flow field, or by using an iterative procedure [1]. Introducing now the quantities

$$\begin{aligned} -\mu &= \phi - \phi_i \\ -\sigma &= \frac{\partial \phi}{\partial n} - \frac{\partial \phi_i}{\partial n} \end{aligned}$$

called respectively *doublet intensity* and *source intensity*, the equation (1.7) becomes

$$\phi(P) = \phi_\infty(P) - \frac{1}{4\pi} \int_{S_B} \left[\sigma \left(\frac{1}{r} \right) - \mu \underline{\nabla} \left(\frac{1}{r} \right) \cdot \underline{n} \right] dS + \frac{1}{4\pi} \int_{S_w} \mu^w \underline{\nabla} \left(\frac{1}{r} \right) \cdot \underline{n} dS \quad (1.10)$$

where as said $\mu^w = \phi_U - \phi_L$ is a known term, related to the doublet intensity at the trailing edge of the body through the Kutta condition. Sources and doublets have a physical meaning too. The thickness effects can be simulated by means of the sources, the non symmetrical conditions, such as those of a 3D aerodynamic body, by means of the doublets.

When solving the equation 1.10 for a specific problem, there is an infinity of combination of singularities distribution that can be assigned to get the solution. Under a numerical point of view, it is convenient to choose the combination that generates the minimum difference in potential between internal and external surfaces of the body, in order to reduce the perturbation introduced by the singularities on the asymptotic stream. Therefore when dealing with thick bodies, in which an internal volume is well defined, the Dirichlet condition on the internal potential is used. In particular we impose that

$$\phi_i = \text{cost} = \phi_\infty$$

If we note that the definition of the sources satisfies the Neumann condition (1.8) by itself, we can now consider them as a known term and the problem reduces to finding the doublets intensity.

When the body we are working with can be considered as thin, the Dirichlet formulation cannot be used. Instead we impose the Neumann condition for the normal velocity component, using the following formulation

$$\underline{n} \cdot \underline{\nabla} \phi(P) = \underline{n} \cdot \underline{\nabla} \phi_\infty(P) - \frac{1}{4\pi} \int_{S_B + S_w} \mu \underline{n} \cdot \underline{\nabla} \left[\frac{\partial}{\partial n} \left(\frac{1}{r} \right) \right] dS \quad (1.11)$$

obtained considering that the normal velocity is continuous through the surface S_B . Furthermore in case of an impermeable body

$$\underline{n} \cdot \underline{\nabla} \phi(P) = 0$$

Therefore solving the equations (1.10) and (1.11) the unknown singularities distribution are obtained, in particular only the doublets needs to be calculated since the sources are imposed through the Neumann condition. The flow field is then computed by deriving the (*now*) known potential. In particular it is possible to determine the velocity in any point of the computational domain. The velocity in a generic point P external to the body can be evaluated using the equation

$$\begin{aligned} \underline{V}(P) = \underline{V}_\infty(P) - \frac{1}{4\pi} \int_{S_B} \left[\sigma \underline{\nabla} \left(\frac{1}{r} \right) - \mu \underline{\nabla} \left(\underline{n} \cdot \underline{\nabla} \frac{1}{r} \right) \right] dS + \\ + \frac{1}{4\pi} \int_{S_w} \mu^w \underline{\nabla} \left(\underline{n} \cdot \underline{\nabla} \frac{1}{r} \right) dS \end{aligned} \quad (1.12)$$

obtained deriving the total potential of equation (1.10). When the point lies on the body it is necessary to use a different formulation. Due to the choice of the sources intensity equal to the normal component of the velocity of perturbation, we can compute the velocity deriving the total potential in a

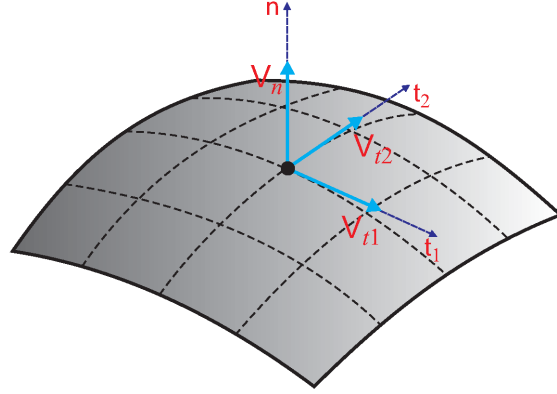


Figure 1.3: Local reference frame for the velocity of perturbation component calculation

local reference frame centered in the point of interest, as shown in figure 1.3. It is in fact possible to evaluate the tangential velocity component deriving the doublets intensity along these directions:

$$\underline{v}(P) = -\frac{\partial \mu}{\partial t_1} \underline{i}_{t_1} - \frac{\partial \mu}{\partial t_2} \underline{i}_{t_2} + \sigma \underline{i}_n \quad (1.13)$$

The total velocity is finally obtained by adding the perturbation velocity to the undisturbed asymptotic one:

$$\underline{V}(P \in body) = \underline{V}_\infty(P) + \underline{v}(P) \quad (1.14)$$

It is then possible to evaluate the pressure field using the Bernoulli theorem and finally compute the forces through a pressure integral or using a Trefftz plane calculation [1].

1.2 Numerical procedure

The mathematical problem introduced above is not of easy resolution, since the boundary conditions (Neumann or Dirichlet) need to be satisfied in each

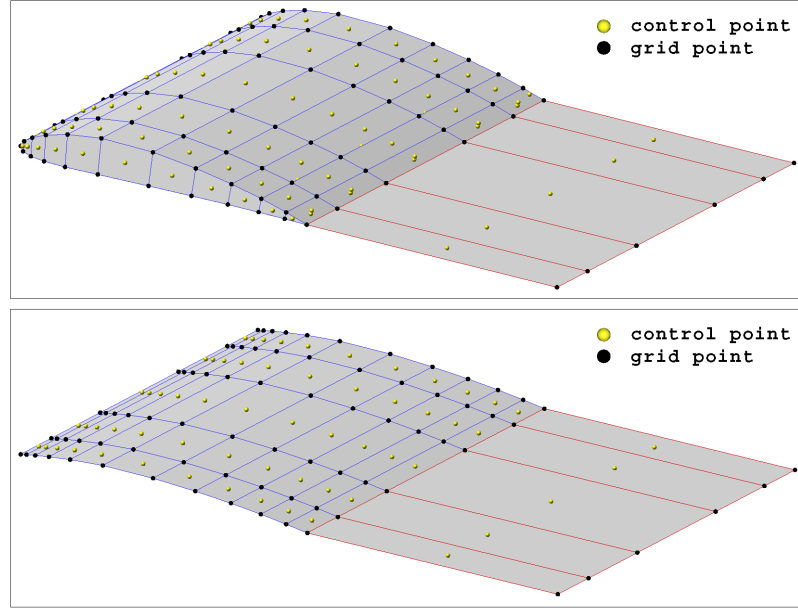


Figure 1.4: An example of a paneled wing surface

point on the surface of the body of interest. Thus the same problem is approached numerically, reducing it to the resolution of an algebraic linear equations system and applying the BCs only in a finite number of points, defined *control points*.

It is therefore necessary to discretize both the surfaces and the singularities distribution. A generic surface is divided in a finite number of regions, named *panels*, described by functions of the kind $z = f(x, y)$ in a local reference frame (figure 1.4). The panels are defined using polynomials which order increases with the accuracy desired to describe the original geometry. Due to the increasing computational cost, the first order polynomial $z = a_0 + b_1x + b_2y$ is the most used, with constant coefficients. The singularity distribution must be subdivided in panels coinciding with the body ones and the singularity strength can be assumed constant, linear or parabolic. Since the global accuracy is determined by the lower order of discretization,

it would be pointless to use a different accuracy for the geometry and singularities. Consequently the simplest discretization results in a quadrilateral panel, defined by plane surface and straight borders, with a constant singularity strength. Using this approach we have a remarkable advantage in the simplicity of calculus but we need a great number of panels to compensate the accuracy loss due to the low polynomials order. However, this is the most used choice for panel methods [2].

Once divided the geometry and the wakes in panels, the centroid of each one is automatically defined and we choose them as control points in which apply the boundary conditions 1.10 and 1.11, respectively if we have a surface with a Dirichlet condition (thick bodies) or a Neumann condition (thin bodies). We can therefore define the equations for every control point of the N_B panels of the physical surfaces. Specifically for each J panel in which the BC is imposed, calling r_J the distance from the panel of which we are evaluating the influence and indicating with N_W the number of wake panels, one obtain

$$\begin{aligned} & \sum_{K=1}^{N_B} \frac{1}{4\pi} \int_{\text{panel } K} \mu_K \underline{n} \cdot \underline{\nabla} \frac{1}{r_J} dS + \sum_{L=1}^{N_W} \frac{1}{4\pi} \int_{\text{panel } L} \mu_L^w \underline{n} \cdot \underline{\nabla} \frac{1}{r_J} dS = \\ & = \sum_{K=1}^{N_B} \frac{1}{4\pi} \int_{\text{panel } K} \sigma_K \frac{1}{r_J} dS \end{aligned} \quad (1.15)$$

for a Dirichlet condition and

$$\begin{aligned} & \sum_{K=1}^{N_B} \underline{n}_J \cdot \frac{1}{4\pi} \int_{\text{panel } K} \mu_K \underline{\nabla} \left(\underline{n} \cdot \underline{\nabla} \frac{1}{r_J} \right) dS + \\ & + \sum_{L=1}^{N_W} \underline{n}_J \cdot \frac{1}{4\pi} \int_{\text{panel } L} \mu_L^w \underline{\nabla} \left(\underline{n} \cdot \underline{\nabla} \frac{1}{r_J} \right) dS = \\ & = \sum_{K=1}^{N_B} \underline{n}_J \cdot \frac{1}{4\pi} \int_{\text{panel } K} \sigma_K \underline{\nabla} \frac{1}{r_J} dS + \underline{n}_J \cdot (\underline{V} - \underline{V}_\infty)_J \end{aligned} \quad (1.16)$$

in case of a Neumann condition. These integrals are referred to the single

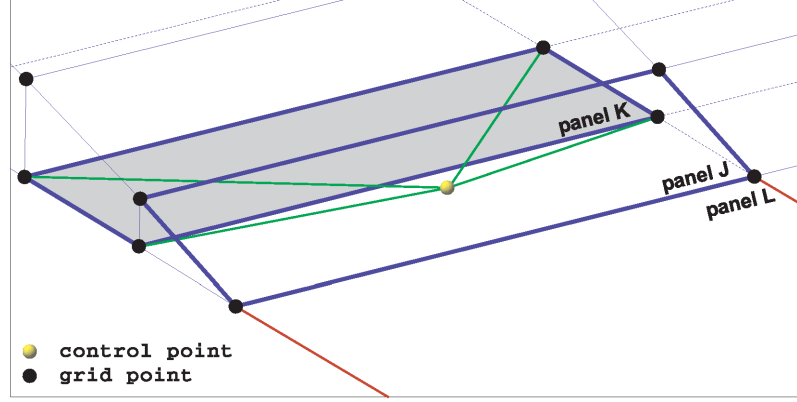


Figure 1.5: Schematization for the influence coefficients definition

panel and represent the influence of each K or L panel evaluated in the control point of a J panel. Using an Hess-Smith procedure [3] these can be replaced by sums referred to the grid points of each panel. For elements with a unitary singularity intensity, the influence only relies on the geometry of the panel and therefore results:

$$C_K^d = \frac{1}{4\pi} \int_{\text{panel } K} \frac{\partial}{\partial n} \left(\frac{1}{r_J} \right) dS \quad B_K^d = \frac{1}{4\pi} \int_{\text{panel } K} \left(\frac{1}{r_J} \right) dS \quad (1.17)$$

$$C_K^n = \underline{n}_J \cdot \frac{1}{4\pi} \int_{\text{panel } K} \underline{\nabla} \left[\frac{\partial}{\partial n} \left(\frac{1}{r_J} \right) \right] dS \quad B_K^n = \underline{n}_J \cdot \frac{1}{4\pi} \int_{\text{panel } K} \underline{\nabla} \left(\frac{1}{r_J} \right) dS \quad (1.18)$$

respectively for constant doublet and source for the K -th panel and where the apices d and n are referred to the type of condition chosen. C_K and B_K are called *influence coefficients* and they are a function of panel geometry and of the distance from the evaluation point. The equations (1.15) and (1.16) can be then rewritten as:

$$\sum_{K=1}^{N_B} C_K^d \mu_K + \sum_{L=1}^{N_W} C_L^d \mu_L^w = \sum_{K=1}^{N_B} B_K^d \sigma_K \quad (1.19)$$

$$\sum_{K=1}^{N_B} C_K^n \mu_K + \sum_{L=1}^{N_W} C_L^n \mu_L^w = \sum_{K=1}^{N_B} B_K^n \sigma_K + \underline{n}_J \cdot (\underline{V} - \underline{V}_\infty)_J \quad (1.20)$$

If we assign the source intensity (for thick bodies) or we impose it to be zero (for thin bodies) we can then calculate the B_K influence coefficients, leaving as unknown only the terms related to the doublets.

Moreover by imposing the Kutta condition, we can relate the wake doublets to the body surface doublets. In fact, if μ_u and μ_l are the doublets intensity of two corresponding panels at the trailing edge on the upper and lower surface of the body and μ_w is the doublet intensity on the adjacent wake panel, by the Kutta condition it results that $\mu_w = \mu_u - \mu_l$. In the same way for thin bodies we have $\mu_w = \mu_u$, since there is no difference between upper and lower surface. The influence of the generic wake panel becomes therefore

$$\begin{aligned} C_L^d \mu_w &= C_L^d (\mu_u - \mu_l) \\ C_L^n \mu_w &= C_L^n \mu_u \end{aligned}$$

and can be replaced in the (1.19) and (1.20) defining

$$A_K = \begin{cases} C_K & K \text{ panel not at the TE} \\ C_K \pm C_L & K \text{ panel located at the TE} \end{cases}$$

and finally obtaining

$$\sum_{K=1}^{N_B} A_K^d \mu_K = \sum_{K=1}^{N_B} B_K^d \sigma_K \quad (1.21)$$

$$\sum_{K=1}^{N_B} A_K^n \mu_K = \sum_{K=1}^{N_B} B_K^n \sigma_K + \underline{n}_J \cdot (\underline{V} - \underline{V}_\infty)_J \quad (1.22)$$

In addition to these equations we need to impose the condition on the wake shape that for a flexible wake consists in imposing that the normal component of velocity in each wake panel control point is equal to zero:

$$\underline{V} \cdot \underline{n}_L = 0 \quad (L = 1, \dots, N_W)$$

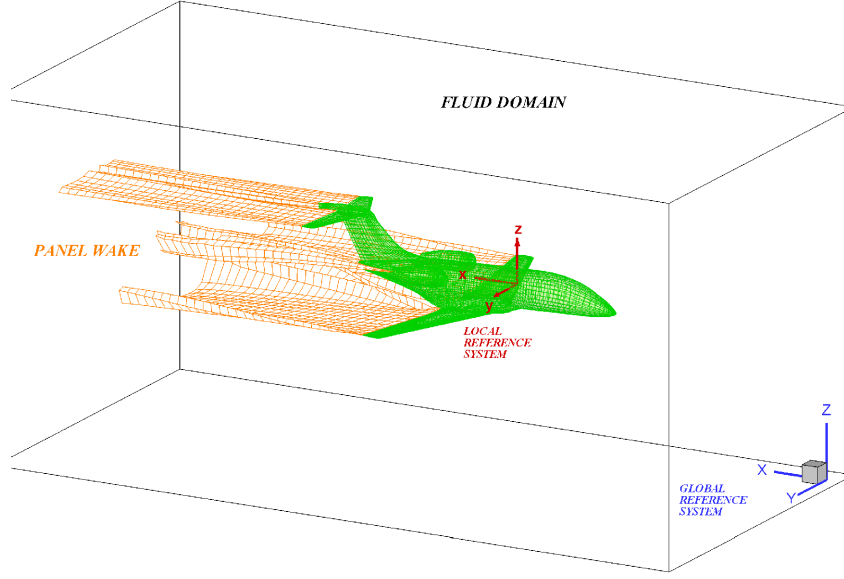


Figure 1.6: Inertial and body fixed reference frame

The equations lead to a N_B linear equations system in N_B unknown terms, nominally the body surface doublets intensity μ_K . The numerical solution of this system is generally stable because the unknown distribution μ is relatively small, since it is related to the perturbation potential only [3].

1.2.1 Unsteady flows case

For an incompressible flow the continuity equation does not take into account the time dependency, which has to be introduced through the boundary conditions. The method developed so far for steady flows can therefore be extended to unsteady problems modifying the boundary condition on the solid surfaces and using an unsteady form of the Bernoulli equation for the pressure calculation. The solution of the potential flow is included in a *time-stepping* loop, starting from $t = 0$; during each time step the intensity of the new wake panels is evaluated using the Kutta condition, while the other wake

panels maintain the same intensity. To modify the body boundary condition it is necessary to introduce an inertial reference frame $(0, X, Y, Z)$ and a body fixed coordinate system $(0, x, y, z)$, as shown in figure 1.6. Supposing the body motion is known, the zero normal flow boundary condition becomes

$$\frac{\partial \phi}{\partial n} = (\underline{V}_\infty + \underline{V}_r + \underline{\Omega} \times \underline{n}) \cdot \underline{n} \quad (1.23)$$

where $\underline{r} = r(x, y, z)$ is the position of a generic point in the body reference frame and \underline{V}_∞ , \underline{V}_r and $\underline{\Omega}$ represent the velocity of the body frame origin in the inertial system, the relative motion of the surface due to deformation of the body, the angular velocity, respectively. If we impose for instance a Dirichlet condition, the equation (1.24) gives us the sources intensity

$$\sigma = -\underline{n} \cdot (\underline{V}_\infty + \underline{V}_r + \underline{\Omega} \times \underline{r}) \quad (1.24)$$

and as seen in the steady case, the wake doublets intensity is related to the intensity of the panels at the trailing edge as stated by the Kutta condition. During every single time step, the wing moves along its flight path and every trailing edge vortex panel sheds a wake panel with a strength (related to the Kutta condition) corresponding to its circulation in the previous time step. It is as if the trailing edge leaves its "tracks" during its pass or, if the body is motionless and surrounded by the stream, the trailing edge is trailed by the flow (1.7). So a new row of wake panels is added to the wake at the separation line and all the preexisting rows of wake panels are convected downstream with the local velocity field in the inertial reference frame at each time step.

During the second time step, the wing is moved along its flight path and each trailing edge vortex panel sheds a wake panel. This first wake sheet, used to account for the vorticity recently shed into the domain from the wing trailing edge, imposes a well defined potential jump at the trailing edge to satisfy the Kutta condition: this condition is used as a boundary condition

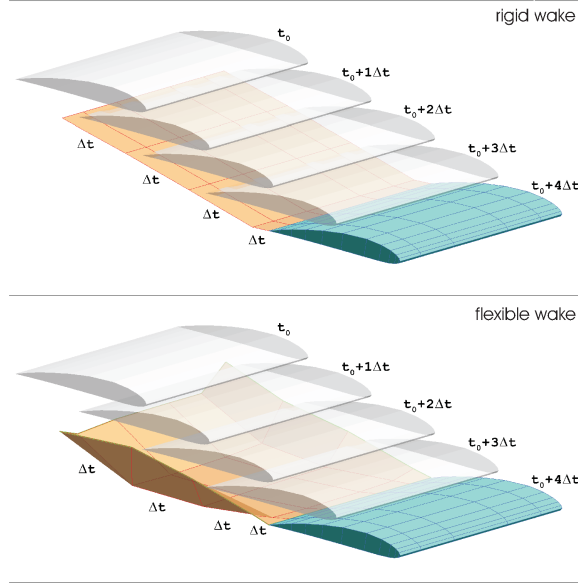


Figure 1.7: Example of rigid and flexible wake

to determine the strength of the doublets to be shed into the first row of a wake. Therefore, at the rising of time the rows successive to the wake panel row, closest to the trailing edge are known. This time stepping methodology may be continued at every single time step in which vortex wake is moved by the local velocity. Thus, unsteady phenomenon like wake rollup may be simulated.

Generally this row of wake panels closest to the trailing edge has a length dimension in the streamwise direction scaled of a factor of $0.2 \div 0.3$ with respect to the natural length equal to $V_\infty \cdot \Delta t$. In PaMS code, the one used for the calculation presented in the next chapters of this work, a value of 0.25 was found to be adequate [4]. This reduced value is a result of the use of vortex rings to model the wake vorticity rather than higher order vorticity distributions [5] [6]. Now referring to the first time step, the boundary condition for the control point of the J -th panel is influenced by the N_B surface

panels and the N_w wake panels generated so far (only one row), and results

$$\sum_{K=1}^{N_B} C_{JK}^d \mu_K + \sum_{L=1}^{N_w} C_{JL}^d \mu_L^w - \sum_{K=1}^{N_B} B_{JK}^d \sigma_K = 0 \quad (1.25)$$

that for the Kutta condition becomes

$$\sum_{K=1}^{N_B} A_{JK}^d \mu_K = \sum_{K=1}^{N_B} B_{JK}^d \sigma_K \quad t = \Delta t \quad (1.26)$$

where only the body surface doublets μ_K are unknown. For every time step following the first, the boundary condition needs to be modified to include the (known) influence of the wake panels previously shed, having

$$\sum_{K=1}^{N_B} A_{JK}^d \mu_K + \sum_{L=1}^{M_w} C_{JL}^d \mu_L^w - \sum_{K=1}^{N_B} B_{JK}^d \sigma_K = 0 \quad t > \Delta t \quad (1.27)$$

where M_w is the number of wake panels that influences the BC: this does not include therefore the new row of wake panels, whose unknown influence is taken into account in the first term of the (1.27). Since the second and the third term are known, the system generated consisting of N_B equations can be solved. If the geometry of the body is not changing in time, the inversion of the matrix has to be done only once; when we have an high number of panels it can be convenient, from a computational cost point of view, to iterate for a new solution in time rather than storing an inverse matrix of large dimensions [2]. For a flexible wake, it is necessary to compute the velocity field in the wake panels corner points and deform them in order to satisfy the equations (1.9). In the case of rigid wake, the problem is linearized by the fact that the wake is imposed and thus the flow field can not influence the wake itself.

The wake modelling presented so far is characterized by using a panel approach for the wake, just like the body surfaces. Another strategy consists in using three dimensional singularity point vortex, named *vortons*, which

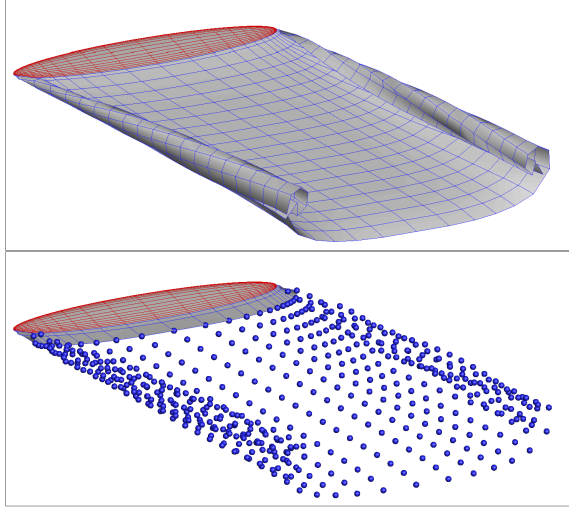


Figure 1.8: Panel wake and vorton wake

are generated by the panels wake. The most important advantage of vorton methods is that they are the solution for body-wake intersection modeling (rotating wing aerodynamics, aircraft in close proximity,...), a critical problem for a classic wake panel approach. Since this kind of problems are not faced in the present dissertation, we will not go deeper in the theory behind vortons methods, but it is important to stress out this strong feature of PaMS code. For further information please refer to [4].

1.2.2 Velocity and forces computation

Once calculated the doublets intensity, it is possible to compute the tangential and normal component of the velocity perturbation on the panel local reference frame

$$v_{t_1} = -\frac{\partial \mu}{\partial t_1} \quad v_{t_2} = -\frac{\partial \mu}{\partial t_2} \quad v_n = \sigma$$

The derivatives are in general evaluated defining a function of the doublets distribution based on a significant number of adjacent control point close to

the point of interest:

$$\hat{\mu} = f(\xi_i, \eta_i, \zeta_i, \mu_i) \quad (i = 1, \dots, n)$$

that is then derived numerically. The total velocity in a generic control point will now result from the sum of the cinematic and perturbation velocity

$$\underline{V}_K = [U(t), V(t), W(t)]_K \cdot (t_1, t_2, n)_K + (v_{t_1}, v_{t_2}, v_n)_K \quad (1.28)$$

The corresponding pressure or pressure coefficient distribution can then be computed, using a discrete form of the Bernoulli unsteady equation

$$p = p_\infty + \frac{1}{2}\rho_\infty(V_\infty^2 - V^2) - \rho_\infty \frac{\mu(t) - \mu(t - \Delta t)}{\Delta t} \quad (1.29)$$

$$C_p = 1 - \frac{V^2}{V_\infty^2} - \frac{\mu(t) - \mu(t - \Delta t)}{\Delta t} \frac{2}{V_\infty^2} \quad (1.30)$$

and finally the force acting on each body

$$\sum_{J=1}^{N_B} p_J \underline{n}_J S_J = \underline{F} \quad (1.31)$$

The forces computation, when it is possible, can also be done with a Trefftz plane analysis approach. This technique is very useful for those surfaces characterized by strong pressure gradients, such as the airfoils, and that can be relatively thin. In this case it results very difficult to obtain an adequate accuracy, especially for the induced drag, using a pressure integral calculation. Using a near-field formulation [7] the Trefftz integral can be evaluated in a region relatively close to the surface, reducing it to a sum referred to the wake panels row adjacent the trailing edge in the discrete form

$$D_i \simeq \sum_{L=1}^{M_w} \mu_L^w w_L \Delta y_L \quad L \simeq 2\rho V_\infty \sum_{L=1}^{M_w} \mu_L^w \Delta y_L \quad (1.32)$$

where w represents the normal component of the velocity perturbation and Δy_J the spanwise lenght of the J -th wake panel.

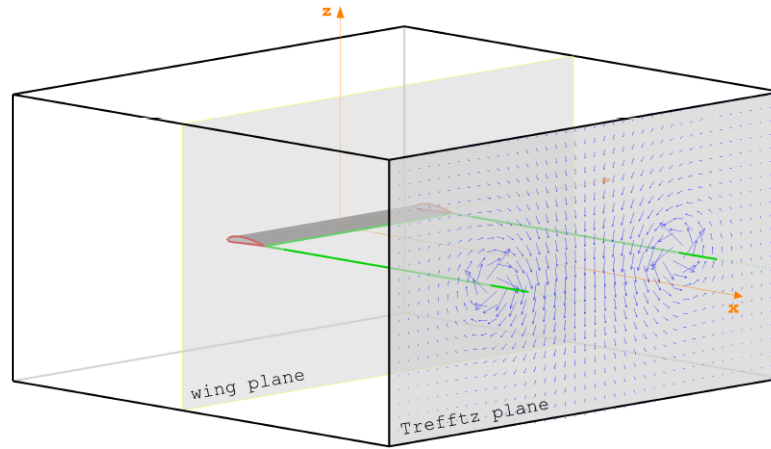


Figure 1.9: Trefftz plane and near-field plane definition

Using this approach it is possible to avoid the problems concerning having a significant number of wake panels, in order to follow the vortex behavior, which would consistently increase the computational cost [2].

Chapter 2

Test Case

The unconventional design of STRATOFly MR3, led to an investigation of different test cases in order to correctly simulate the vehicle case study with the selected low speed code. Specifically PaMS capability on internal flows simulation was investigated for the engine flow characterization and a study on a delta wing was carried out with the purpose of exploring the application of Polhamus analogy to the panel method solution, required to take into account the vortex lift contribution.

2.1 Subsonic Diffuser

The first test case presented was performed on a subsonic diffuser. Starting from the test reported in [4], dealing with the flow inside a constant section pipe, a linearly varying section duct was studied in order to attest PaMS capability in simulating the similar flow occurring inside of STRATOFly engine. The diffuser main geometric properties have been reported in table 2.1. The most crucial aspect to be considered is the necessity of imposing the value of the mass flow rate passing through the inlet and outlet sections

Diffuser Length [m]	5
Inlet Surface Area [m^2]	4.5
Outlet Surface Area [m^2]	12.5

Table 2.1: Diffuser main geometric properties

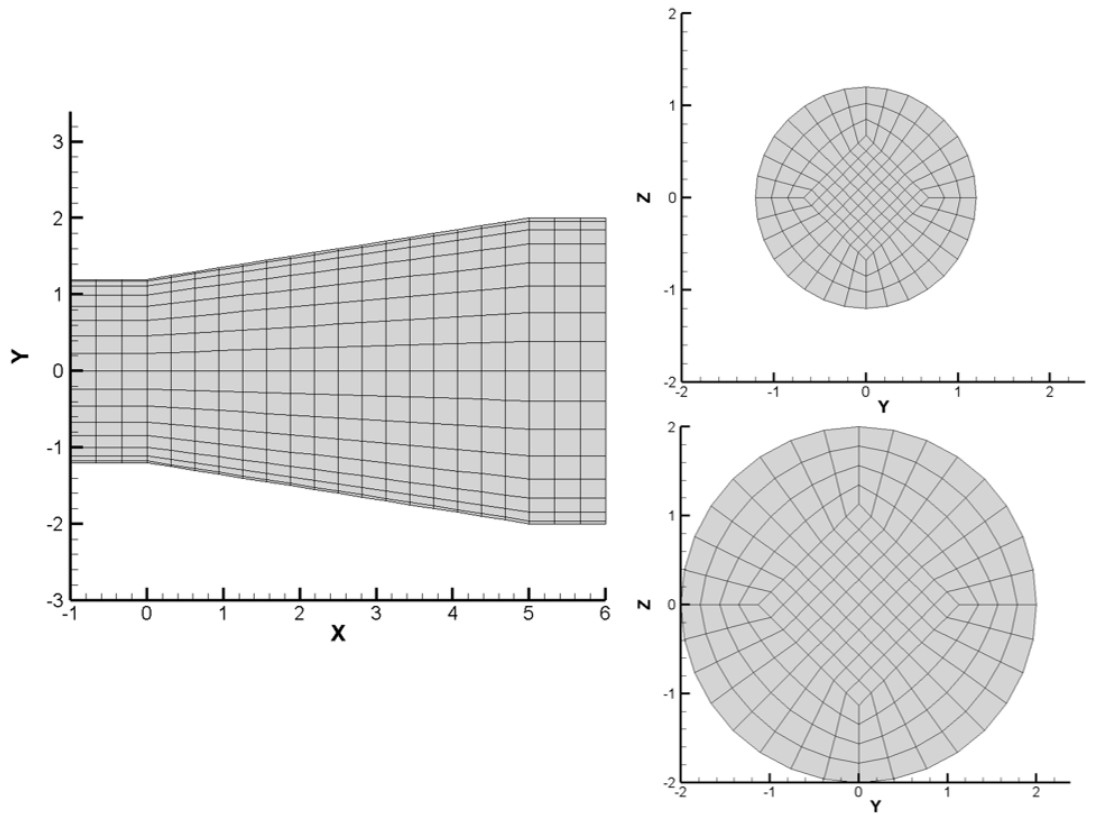


Figure 2.1: Diffuser Wall, Inlet and Outlet surface grid

```

-----
&GEOIN   geoname="inlet3_quad.geo"                                icb=1
&GEOIN   orient   =-1      orignumb ='N'      maxang=100.0      &END
&SCALE   sclfac(1)=1.0      sclfac(2)=1.0      sclfac(3)=1.0      &END
&KWAKE   ang=140.      tmsfac=1.0      kwnumb   ='N'      &END
&KWAKE   nkwtspan =200      nkwtspan =200      nkwtspan =200      &END
&KWAKE   xanru = 0.      yanru = 0.      zanru = 0.      &END
&BC       bctype(1)='D'      bctype(2)='R'      bctype(3)='I'      &END
&BC       bcnvel =1.0      bcidou  ='Y'      &END
&BCLIM   corerad  =0.1      coremod   ='R'      pt2wknd  =0.      &END
-----

```

Figure 2.2: PaMS input file (DATAIN) with a $V = 1 \text{ m/s}$ normal velocity *bcnvel* and equipotential surface *bcidou* enforcement

of the duct, to correctly simulate the flow. The mass flow rate was imposed in terms of a normal velocity in two equipotential surfaces, corresponding to the inlet and outlet sections, combining PaMS features *bcnvel* and *bcidou* [4] [1]. The to be imposed velocity values were calculated applying the continuity equation

$$\dot{m} = \rho V A = \text{cost} \quad (2.1)$$

to the considered geometry. In order to control the numerical error, additionally the inlet and outlet sections were extended in the streamwise direction. The same surface mesh was employed to carry out also an Euler calculation using *Fluent*.

In figure 2.4 both PaMS and CFD results have been reported and compared to the 1-D solution. PaMS velocity was extracted on both the wall and the axis of the duct through an out-body points calculation. The results show a very good agreement with both methods, despite some differences close to the outlet section. Indeed the three-dimensionality of the flow results in a velocity variation even in the radial direction, as shown in figure 2.4 where the radial velocity was reported in the $X/L = 1$ section.

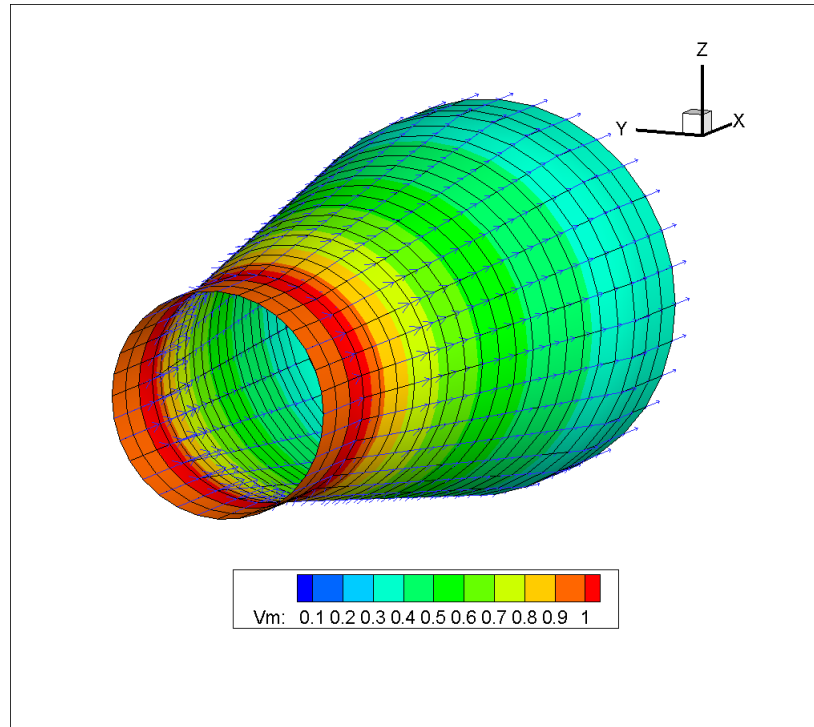


Figure 2.3: Velocity contour and vectors on Diffuser wall

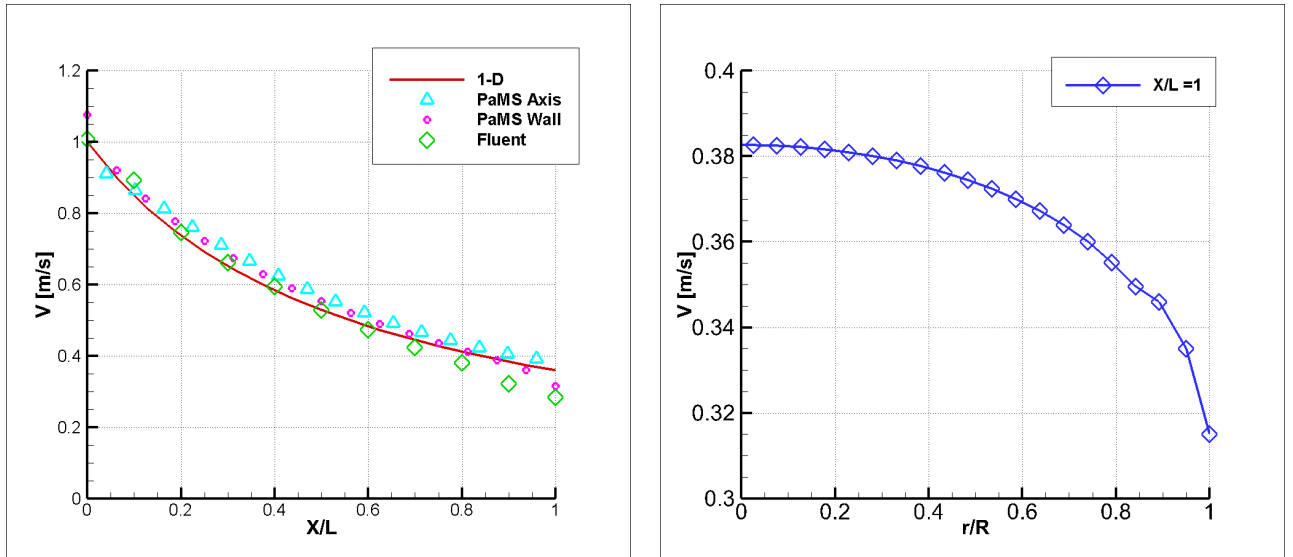


Figure 2.4: PaMS vs Fluent velocity plot compared to the 1-D solution (*left*),
PaMS radial velocity distribution in the outlet section $X/L = 1$ (*right*)

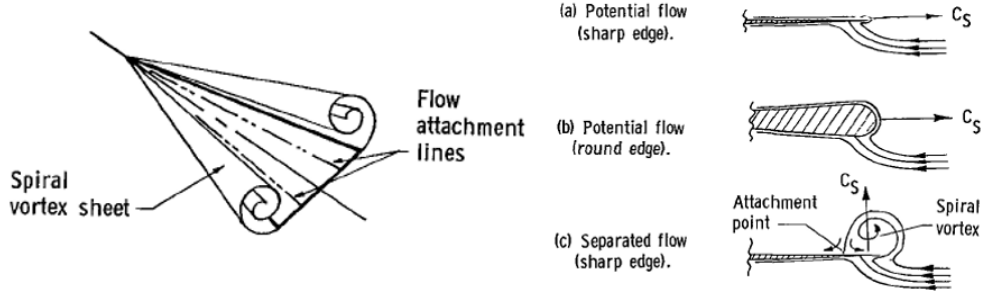


Figure 2.5: Delta Wing Vortex flow (*left*) and leading edge flow conditions (*right*)

2.2 Delta Wing

A second test case was conducted on a delta wing, mostly to attest PaMS capability in the application of Polhamus analogy. The delta wing aerodynamics results indeed to be dominated by vortex structures [8] [9], which a panel method for potential flow is not able to capture. The idea Polhamus proposed was that, due to flow separation at the wing leading edge, the suction force generated makes an upwards 90° turn. Such rotation occurring round the separation bubble of a thin leading edge, converts the potential axial suction force in a lifting force, of an essentially viscous nature (figure 2.5). The vortex flow not only increases the lift but changes the distribution of lift rather drastically. Because of the flow separation at the sharp leading edge, the pressure peaks at the leading edges predicted by potential-flow theory are not developed, but peaks are developed inboard of the leading edges due to the separated vortex sheets [8]. The mesh was therefore created with a particular focus on the wing edges (figure 2.7). It is in fact necessary to have an as homogeneous as possible grid in order to correctly extract the leading edge suction force and consequently apply the analogy.

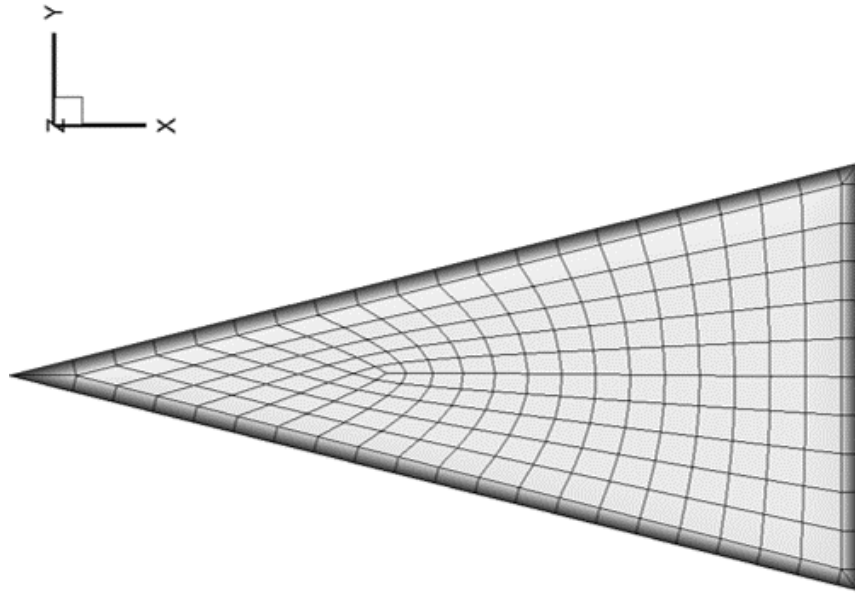


Figure 2.6: Delta Wing mesh upper view

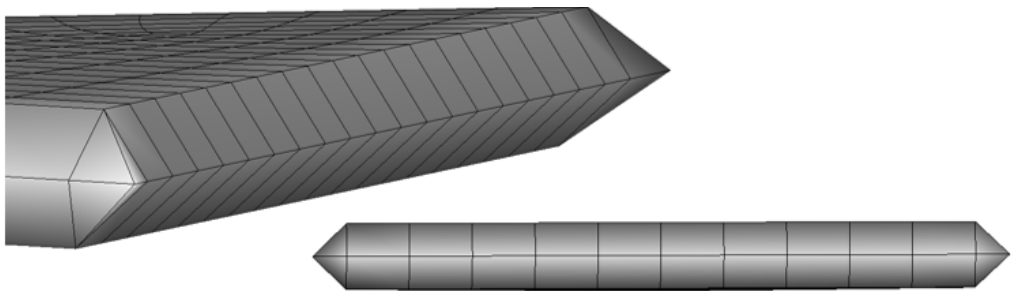


Figure 2.7: Delta Wing mesh detail on Leading Edge (*left*) and Trailing Edge (*right*), Z scale factor = 10

AR [-]	1
Wing Span [m]	2
Planform [m^2]	4

Table 2.2: Delta Wing main geometric properties

The vortex force is clearly visible in figure 2.8, whereas figure 2.9 shows how the expansion peaks on the wing leading edge were captured using PaMS. Extracting the pressure evaluated on the leading edge line grid points, it is possible to evaluate the vortex force contribution by integrating it over the leading edge surface. Also a sensitivity study in relation to the leading edge surface percentage considered was consequently carried out, since the effectively leading edge area affected by the suction force is not known uniquely, and was reported in figure 2.11.

The results have been compared to the NASA study developed in [10]. The potential lift contribution was compared to PaMS results for both Pressure integral and Trefftz solutions: Trefftz result is in good agreement with NASA up to 20° of incidence, whereas pressure integral better follows the potential lift trend but results to be underestimated by PaMS (figure 2.10). The total lift coefficient was finally reported in figure 2.12, considering Trefftz solution for the potential contribution. The procedure followed in this test case was consequently replicated on STRATOFly MR3 to take into account the vortex force contribution.

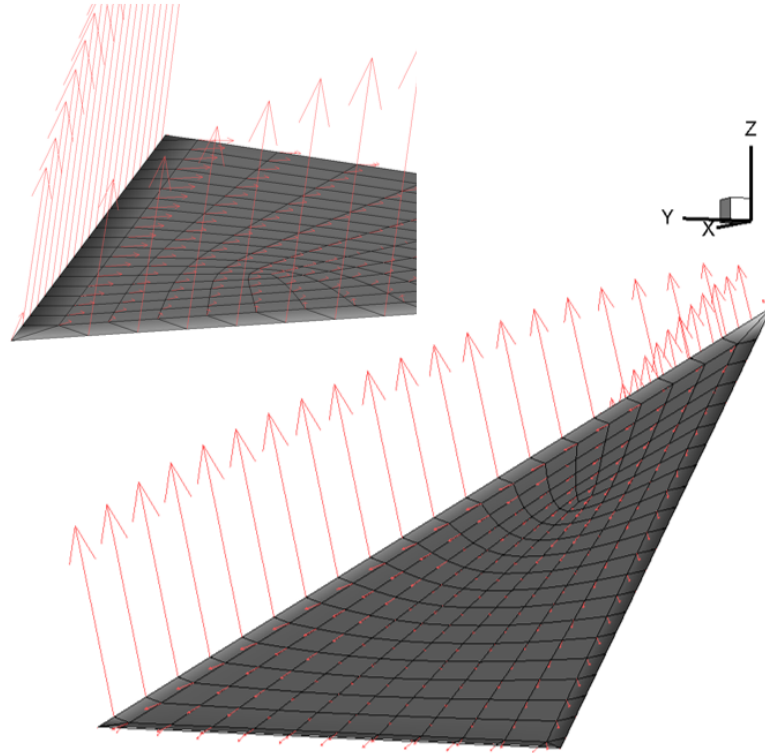
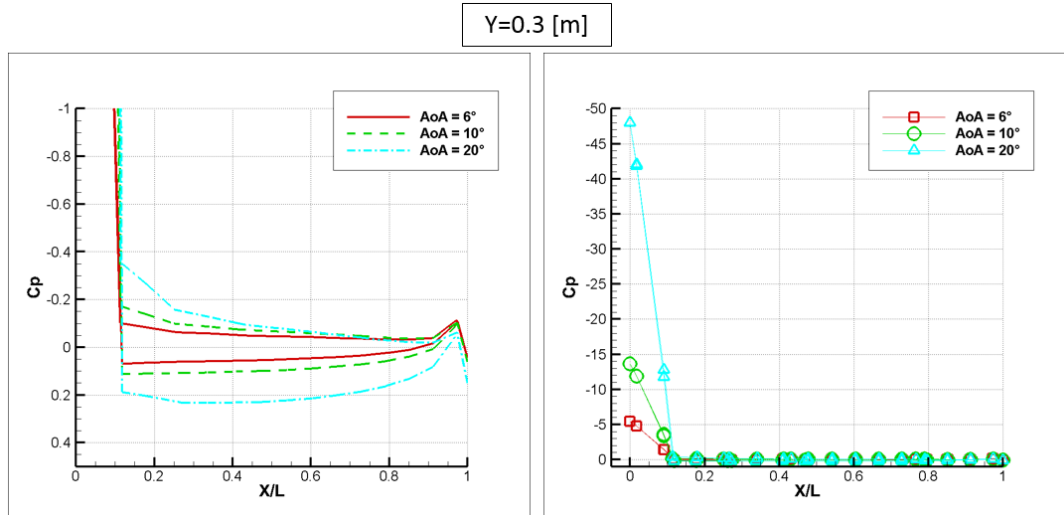


Figure 2.8: Leading Edge Vortex Force captured using PaMS

Figure 2.9: Pressure Coefficient distribution for different AoA (*left*), LE expansion peaks in detail (*right*), $Y = 0.3 [m]$

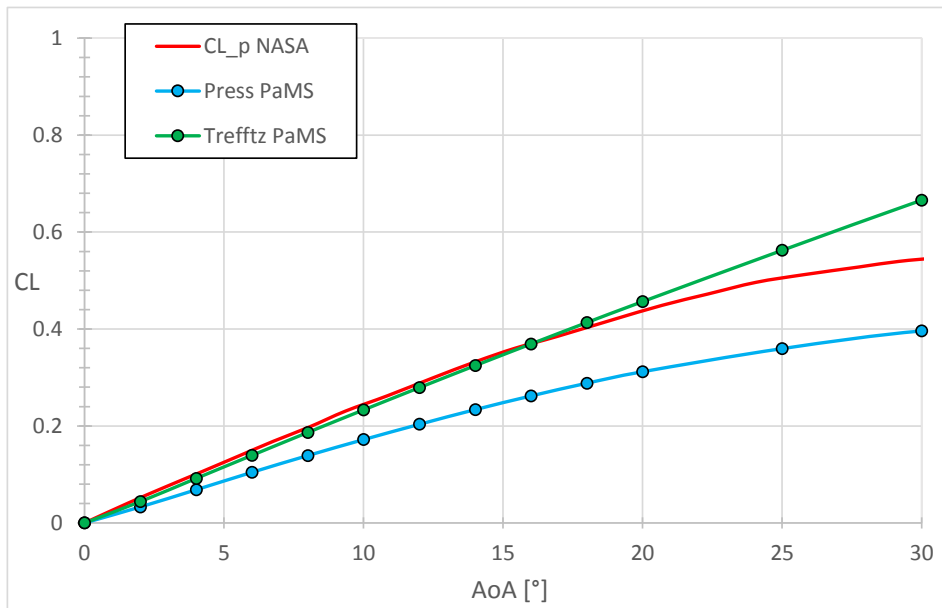


Figure 2.10: PaMS Lift coefficient calculated as Pressure integral and with Trefftz formulation vs NASA [10] potential lift contribution

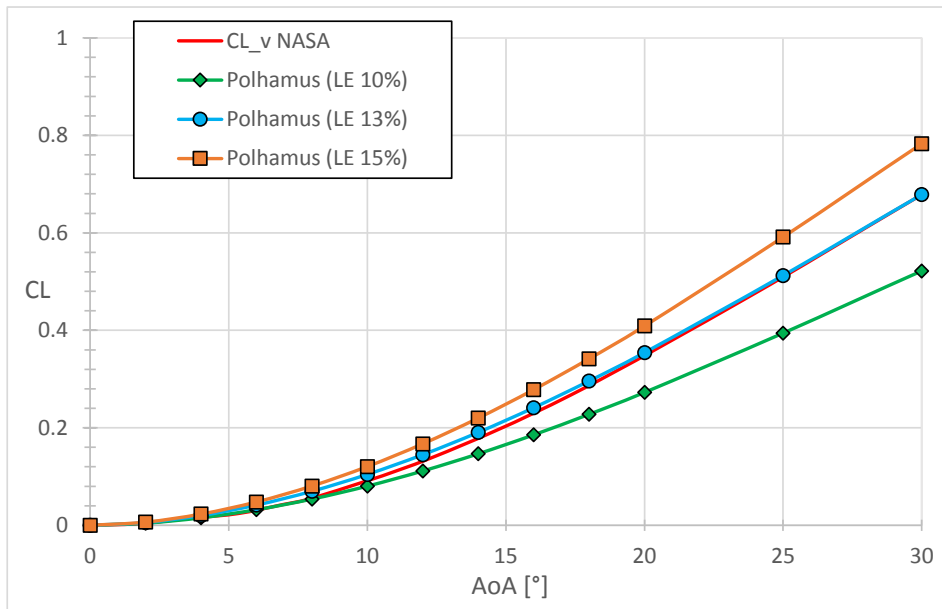


Figure 2.11: Vortex Lift coefficient sensitivity study with respect to the LE surface percentage considered vs NASA [10] vortex lift contribution

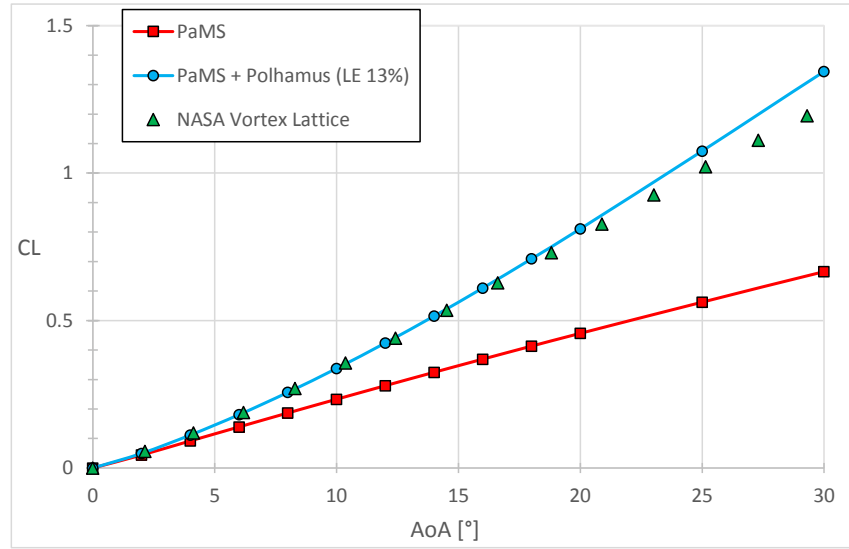


Figure 2.12: PaMS Lift coefficient with Polhamus correction for a 13% LE surface vs NASA [10] Total lift coefficient

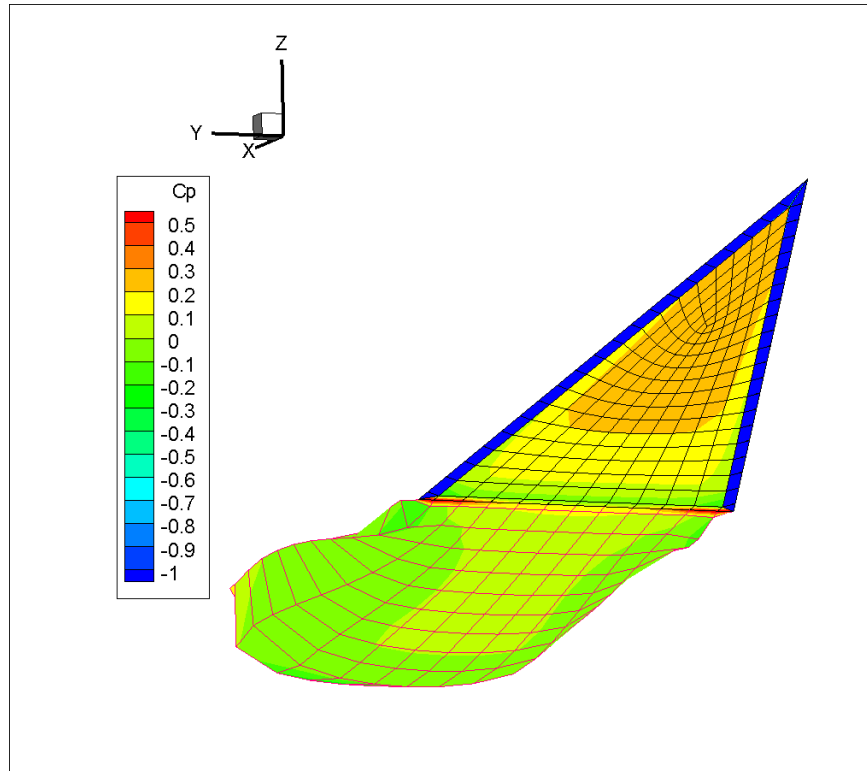


Figure 2.13: Pressure coefficient contour for $AoA = 20^\circ$

Chapter 3

The Hypersonic Aircraft STRATOFLY

Once PaMS code capability of dealing with STRATOFLY MR3 challenging design was attested throughout several test cases, the actual vehicle was studied. After an overview on the STRATOFLY project, the analysis setup and results of both CIRA Euler CFD calculations and Panel Method approach will be presented and discussed in the present chapter.

3.1 About STRATOFLY

The STRATOFLY project has received funding from the European Union's Horizon 2020 research and innovation program and studies the feasibility of high-speed passenger stratospheric flight. Technological, environmental and economic factors, that allow the sustainability of new air space's exploitation, are taken into account, drastically reducing transfer time, emissions and noise, and guaranteeing the required safety levels [11]. The main project objectives are to refine the design and the concept of operations of



Figure 3.1: The reference vehicle LAPCAT-II MR2.4 (*left*) and STRATOFly MR3 concept (*right*)

the LAPCAT-II MR2.4, that has been selected as reference vehicle, and to reach the ambitious goal of TRL=6 (technology demonstrated in relevant environment) by 2035 for the concept [12], developing crucial technologies which may represent a step forward for future reusable space transportation systems. STRATOFly hypersonic vehicle will fly at Mach 8 above 30 km of altitude, performing an antipodal civil passenger transport mission. The route from Bruxelles to Sydney has been chosen as reference with a mission profile shown in figure 3.2, a range of about 18700 km and a flight duration of about three hours. From the operational point of view it was assumed that it is not possible to have a supersonic leg of the trajectory over land in order to avoid sonic boom generation close to inhabited areas. This can have a significant impact on the length of the to be flown trajectory [13]. The purpose of current work in the frame of STRATOFly project, is to investigate the subsonic Mach numbers range, in the specific from $M = 0$ to $M = 0.7$, using a panel method (specifically PaMS) in order to define an aerodynamic database for lift, induced drag and pitching moment coefficients. This will be useful, especially in the current preliminary design phase, to evaluate the vehicle characteristics and to carry out trajectory simulations

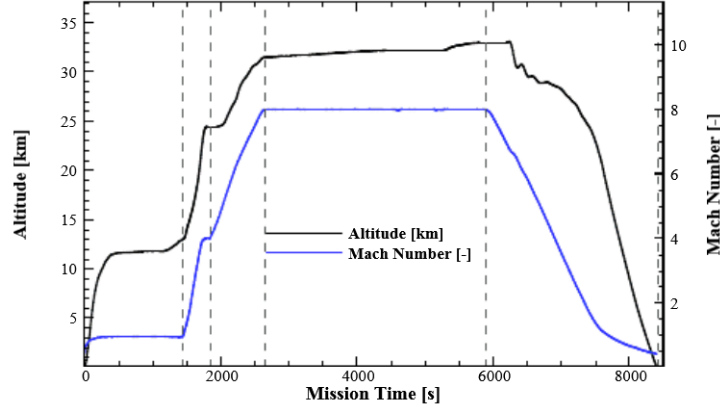


Figure 3.2: Flight Altitude and Flight Mach Number vs Mission Time

and optimizations together with the propulsive subsystem modeling.

3.1.1 Geometry

The STRATOFly vehicle concept is characterized by an hypersonic wa-verider configuration in order to maximize the lift-to-drag ratio L/D , and can be considered as a refinement of the LAPCAT MR2 concept. Both vehicles are indeed characterized by a similar shape, and the main geometric and mass characteristics are resumed in table 3.1. As described in [13], as a

Length [m]	94
Wing Span [m]	41
Planform [m^2]	2491
AR [-]	0.68
Wing Max Thickness	4.8%
GTOW [ton]	400 [14]

Table 3.1: STRATOFly MR3 main geometric and mass properties

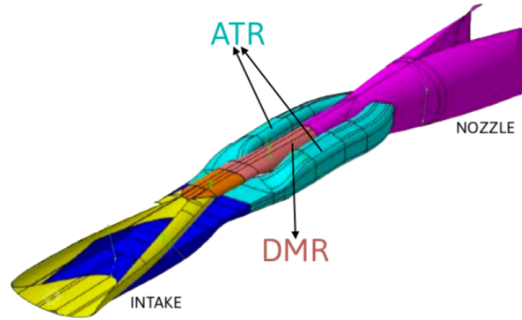


Figure 3.3: Air-Turbo Rocket and Dual Mode Ramjet/Scramjet propulsion unit

start for the design, the overall internal flow path and the different components for the propulsion unit were laid out. Consequently, starting from the elliptical intake lip contour, a waverider configuration was constructed. The current vehicle is 94 m long and has a wingspan of 41 m , it hosts a passenger's compartment accommodating 300 passengers and an highly integrated dorsal mounted combined propulsion system. As shown in figure 3.3 it is characterized by a merging of six Air-Turbo-Rocket (ATR) engines, accelerating the vehicle up to Mach 4, and one Dual-Mode-Ramjet/Scramjet (DMR) engine, operating from $M = 4$ to $M = 8$. Considering its high energy content, liquid hydrogen has been selected as propellant, to be stored in cryogenic integrated bubble tanks. As far as the external vehicle layout, a review of the empennages (elevators/ailerons, canards and vertical tail) design and sizing has been carried out, together with an in-depth investigation of the most suitable radius of curvature to be used as rounding for the various leading edges [12]. Following typical engineering procedures for a conceptual design phase of such vehicles, a different configuration in terms of horizontal and vertical empennages with related control surfaces has been obtained [15] (see

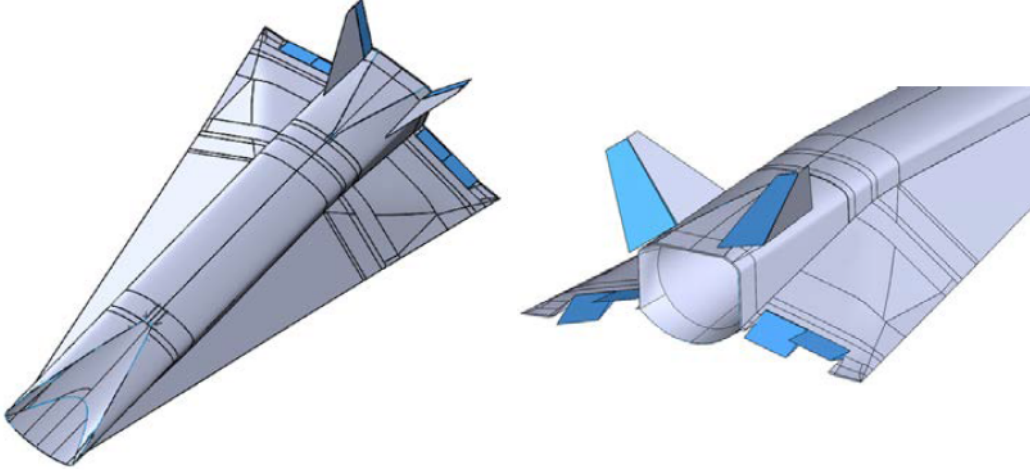


Figure 3.4: STRATOFly MR3 vehicle configuration with empennages and flight control surfaces definition

figure 3.4). For the analysis performed in current work, only the Dual Mode Ramjet engine (intake, combustion chamber, nozzle) was considered, as it is possible to see in figure 3.5.

3.2 CFD - CIRA

CFD calculations have been carried out at CIRA (*Centro Italiano Ricerche Aerospaziali*) in the entire range of Mach numbers from $M = 0$ up to $M = 8$. For the current work, we will only refer to the subsonic range of Mach numbers. In particular the commercial code *Fluent* was used to perform Euler calculations on full STRATOFly configuration, specifically external geometry together with the scramjet engine. There has not been a grid independence analysis of the solution since we are still in a preliminary stage, thus an unstructured mesh of about $0.9 \cdot 10^6$ cells was chosen, as shown in figure 3.6. In table 3.2 are in addition reported the farfield conditions used for *Fluent* setup. The flow field is clearly dominated by vortex structures,

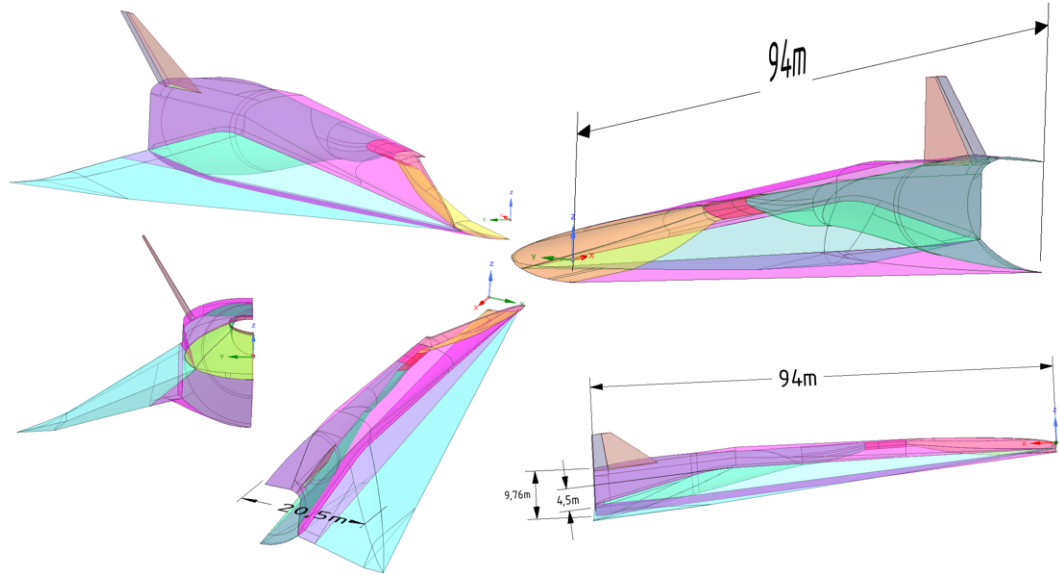


Figure 3.5: STRATOFly concept vehicle half body configuration

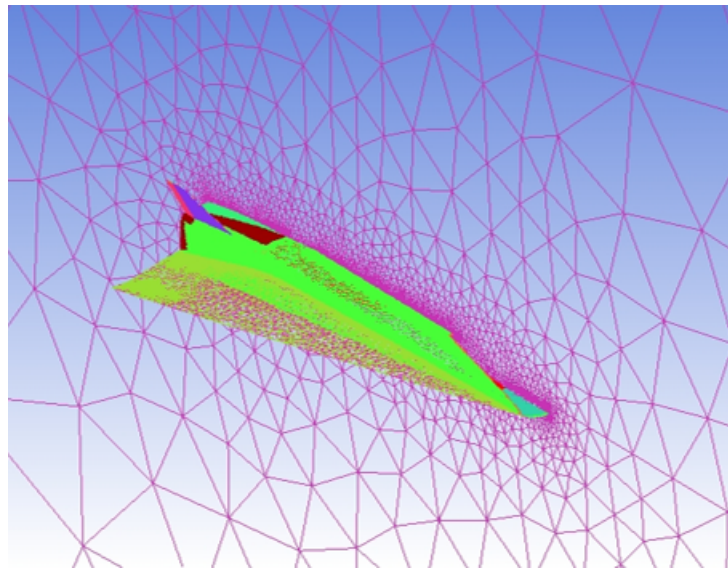
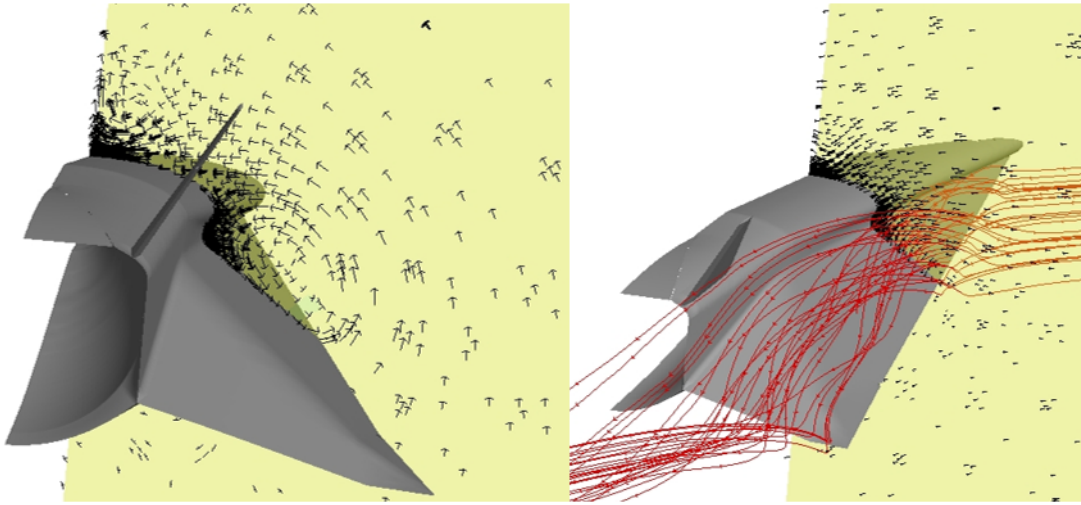


Figure 3.6: CIRA Euler *Fluent* grid, $0.9 \cdot 10^6$ cells

Mach [-]	Press [Pa]	Temp [K]	Dens [kg/m^3]	Sound Sp [m/s]	Vel [m/s]
0.3	101696	291	1.217	342	103
0.5	101696	291	1.217	342	171
0.7	89363	284	1.094	338	237

Table 3.2: CIRA Euler Farfield conditions for *Fluent* setupFigure 3.7: Vortex structures extracted from CFD calculations for $AoA = 6^\circ$

originated by the delta wing leading edge. The vortex lift contribution is consequently essential to characterize the wing aerodynamics, especially at medium-high incidence, and it is therefore necessary to apply Polhamus analogy to the panel method calculation to take it into account. Figure 3.7 shows the vortices generated at $AoA = 6^\circ$.

3.3 PaMS (Panel Method Solver)

In order compare the CFD results, a panel method was chosen to study the vehicle aerodynamic behavior. The choice was mostly driven by the

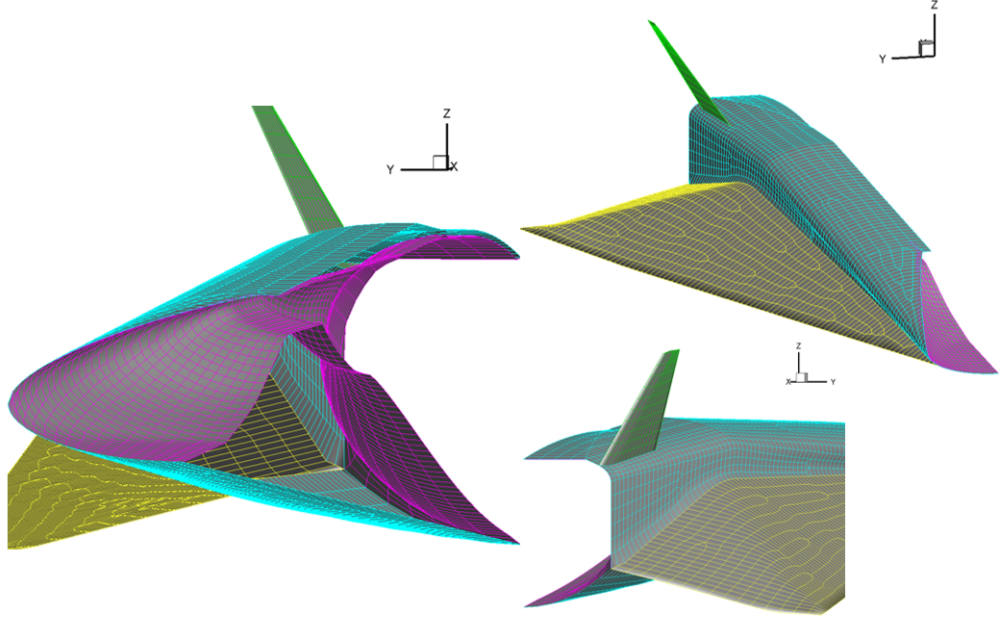


Figure 3.8: STRATOFly full surface mesh

necessity of having a tool that could rapidly carry out simulations, with a lower computational cost with respect to the CFD solver and with the advantage of easily updating the aerodynamic database for any new needed design condition. The analysis were made using the already mentioned PaMS code [4] for $M = 0$ ($V_\infty = 1 \text{ m/s}$) in the range of angles of attack from -6° to 6° and have been compared to the CFD results, with a particular focus on $M = 0.3$. In order to estimate the vortex lift, phenomenon that controls the delta wing aerodynamics, the successfully tested Polhamus analogy was used (see Chapter 2).

3.3.1 Meshing

The software *Patran* was used to generate a surface mesh of the geometry. As seen in figure 3.8 finally an almost structured grid was obtained, with

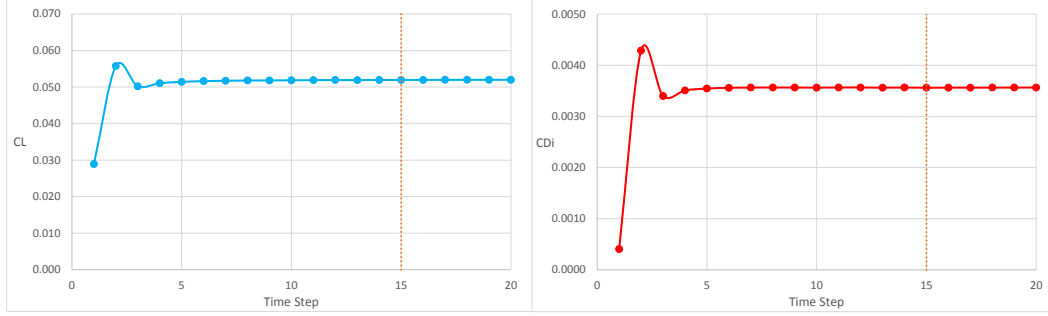


Figure 3.9: Lift (*left*) and Induced Drag (*right*) coefficients of the wing convergence curves

an average element length of 1 m and a total of about 5700 quad elements. The importance of an homogeneous and uniform grid relies on the necessity of correctly capturing the delta wing aerodynamics, in particular concerning the leading edge area.

3.3.2 Setup

Even though the code has an inbuilt compressibility correction, all the tests were performed for an asymptotic velocity $V_\infty = 1\text{ m/s}$ in order to reduce the doublets intensity and lower the calculation time. The compressibility effects were taken into account in the post-processing, using the Prandtl-Glauert correction [2]

$$C_x|_M = \frac{C_x|_{M=0}}{\sqrt{1 - M^2}} \quad (3.1)$$

A convergence check was moreover necessary, in order to choose the correct simulation time. In particular in figure 3.9 the convergence curves of both the lift and induced drag coefficient of the wing have been reported, used as reference for wake cut-off. Finally a total of 15 time steps was chosen, since the change in magnitude between each TS became lower than 0.1%. In table 3.3 the main properties of the wake are resumed.

3.3.3 Internal and External Flow

The first tests were carried out on the full configuration (external geometry and engine together). In order to correctly simulate the flow inside the engine, as seen in the test case reported in Chapter 2, the Mass Flow Rate in the inlet and outlet sections needs to be imposed in terms of a normal velocity. The effectively captured mass flow rate in the inlet section was not known *a priori*, therefore a sensitivity study of the aerodynamics coefficients with respect to the mass flow was carried out. The reference value used (*i.e.* MFR 100%) was extracted from the CFD calculations, and therefore for each angle of attack the influence of a 20% reduction and increase in mass flow rate with respect to this value was evaluated. As shown in figure 3.10 it can be noticed that the mass flow rate has a very slight influence over the lift and consequently the pitching moment coefficient for a fixed angle of attack. Additionally since we were interested in the external flow characterization and the objective of the study was to use an independent method with respect to the CFD approach, tests on the geometry without the engine were carried out, in order not to rely on the mass flow rate enforcement.

3.3.4 External Flow

The geometry was adapted as shown in figure 3.11. The engine was removed with the purpose of eliminating the mass flow rate dependency. As seen in

Wake Model	Rigid
Time Step Δt	5 s
Total Simulation Time	75 s

Table 3.3: PaMS Wake model

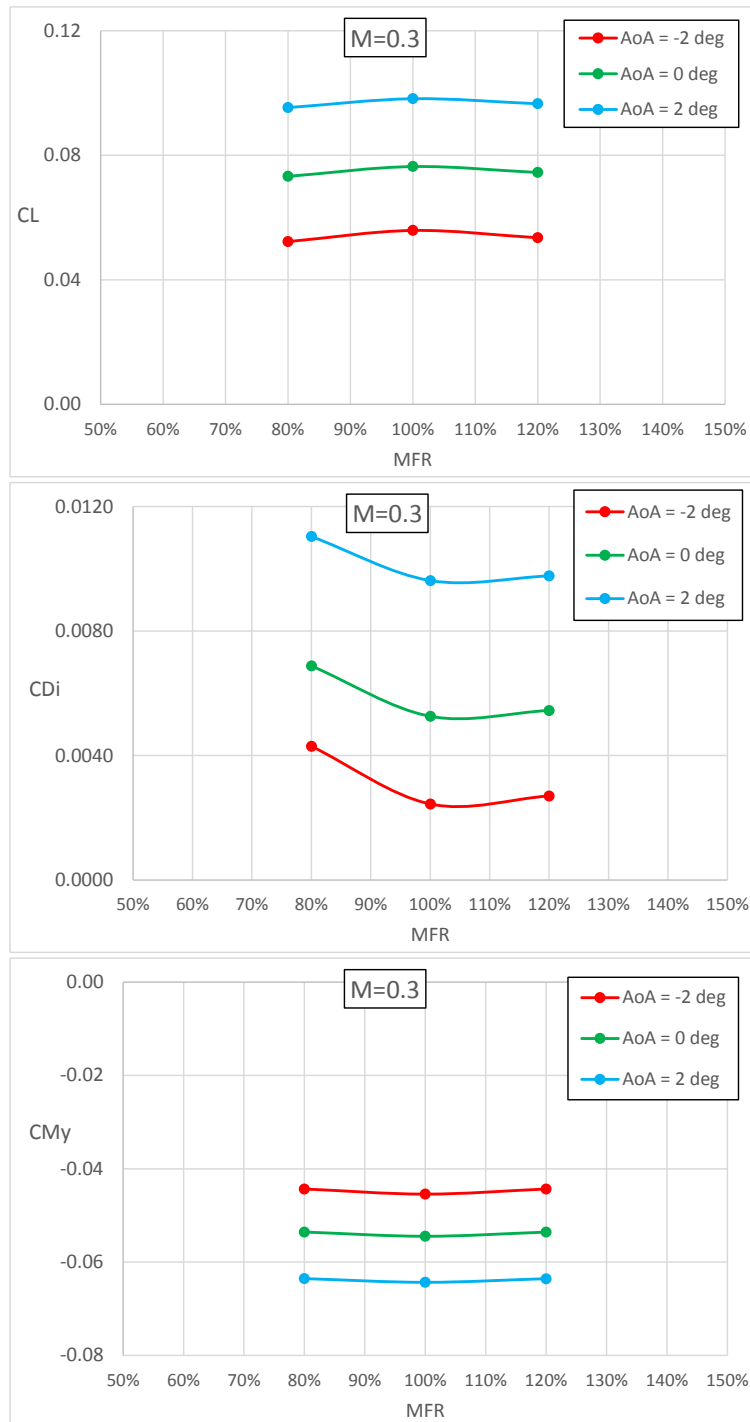


Figure 3.10: Lift (*up*), Induced Drag (*mid*) and Pitching Moment (*down*)
Mass Flow Rate sensitivity study

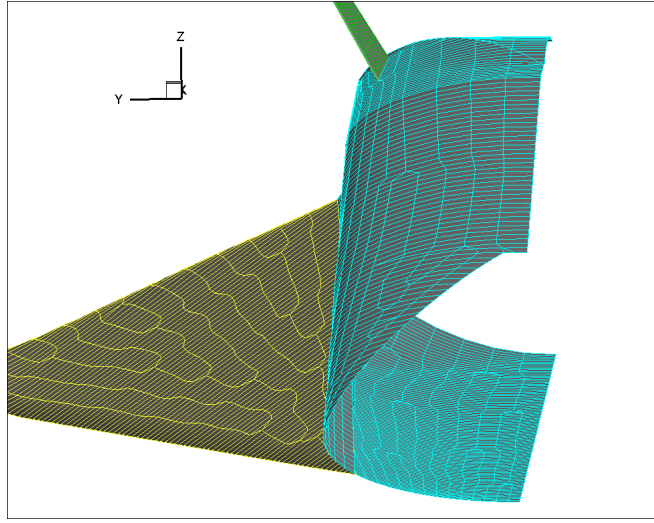
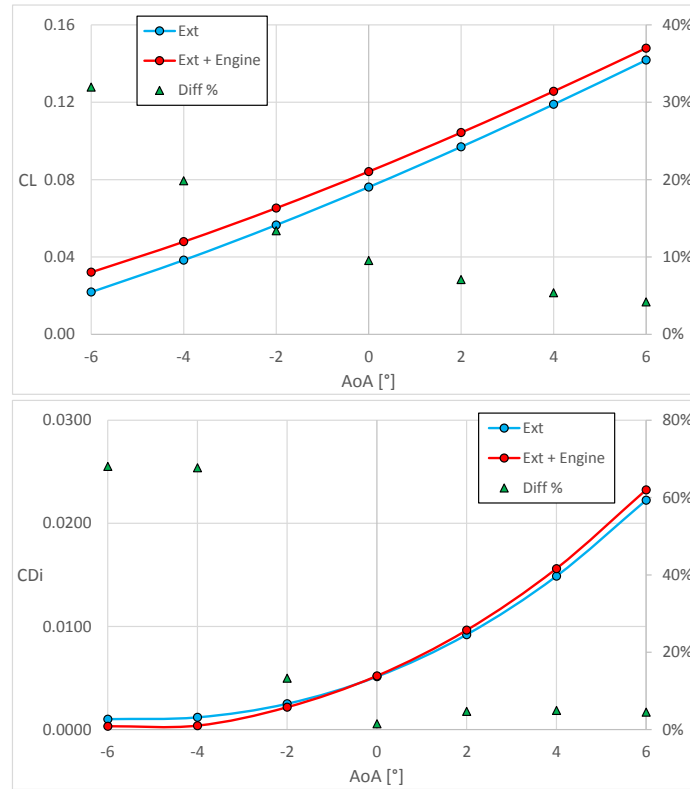


Figure 3.11: STRATOFly surface grid without engine

Figure 3.12: Comparison between Full configuration (Ext + Engine) and External, $M = 0$ (only the external flow field is considered)

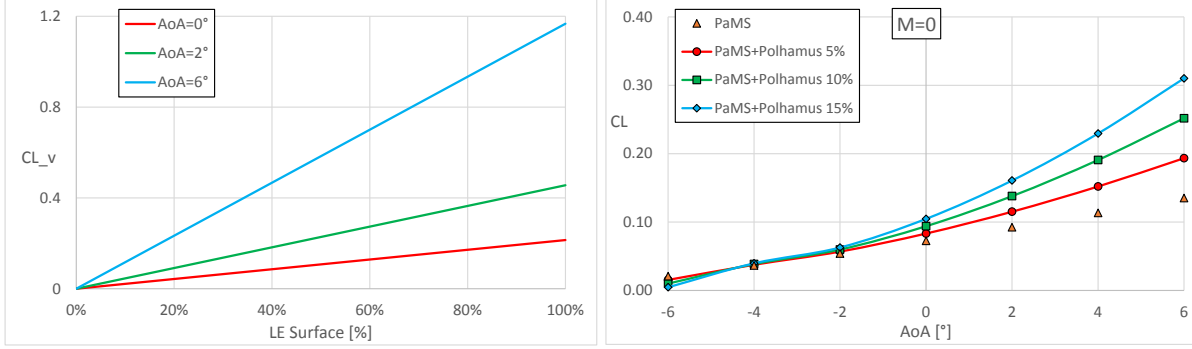


Figure 3.13: Vortex Lift coefficient sensitivity study (*left*) and Lift coefficient for different LE surface percentages (*right*), $M = 0$

figure 3.12 the difference between the results decreases with an increasing angle of attack. Since we are interested in the external flow, it was assumed that the influence of the engine on the external flow field could be neglected. As shown in figure 3.7 in the CFD section, the flow field is clearly dominated by the vortices shed by the delta wing. To take into account the vortex lift contribution, Polhamus analogy was applied, since it is not captured by the panel method. The two rows of panels joining at the corner of the leading edge were chosen as the total LE surface. Since the effective leading edge area affected by the suction force is not known uniquely, a sensitivity study with respect to the leading edge surface percentage considered was performed (figure 3.13). In the results section, the solutions for a 10% LE surface have been reported.

3.4 Results

Contours for both velocity and pressure coefficients have been reported in figures 3.14 - 3.15 - 3.16 respectively for angle of attack $AoA = -6^\circ$, $AoA = 0^\circ$ and $AoA = 6^\circ$. In particular it is possible to notice in figure 3.17 in relation

to $AoA = 0^\circ$ the expansion peak reached on the wing upper surface and the stagnation area on the inlet leading edge.

The pressure coefficient profile for several wing sections at $AoA = 0^\circ$ have been then compared to CFD calculations. The results show a good agreement between the two methods, although differences can be noticed in the leading edge area and especially at the trailing edge. The reason, as said, relies on the different equations the two methods are based on, resulting in a different pressure distribution since the vortex structures are not expected to be simulated by the panel method approach. The differences in pressure integral are consistent with the lower aerodynamic force resulting from PaMS. Lift, induced drag and pitching moment coefficients were reported for both PaMS and CIRA Euler calculations at $M = 0.3$ (figure 3.22). The curves show an almost perfect agreement in the zero lift area, although the difference increases with the angle of incidence. Polhamus contribution related to the vortex lift is essential at higher angles of attack, as the leading edge vortex intensifies. In particular for this comparisons a 10% leading edge surface was considered. Concerning the CFD, two different Euler calculations were carried out, respectively with a *1st* and a *2nd* order spatial discretization. It is interesting to notice that the *2nd* order solution tends to the direction of a better comparison with PaMS results. In addition, the longitudinal static stability is achieved in any flight condition studied ($C_M|_\alpha < 0$). In figure 3.23 and 3.24 also the coefficients curves for $M = 0.5$ and $M = 0.7$ have been reported.

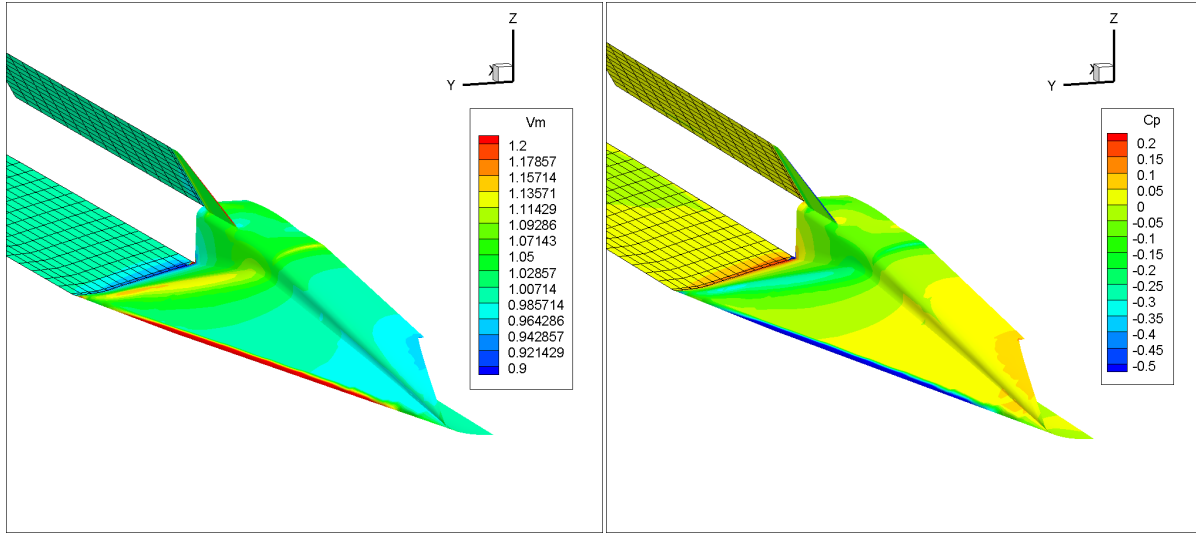


Figure 3.14: Velocity (*left*) and Pressure Coefficient (*right*) contours for $AoA = -6^\circ$, $M = 0$

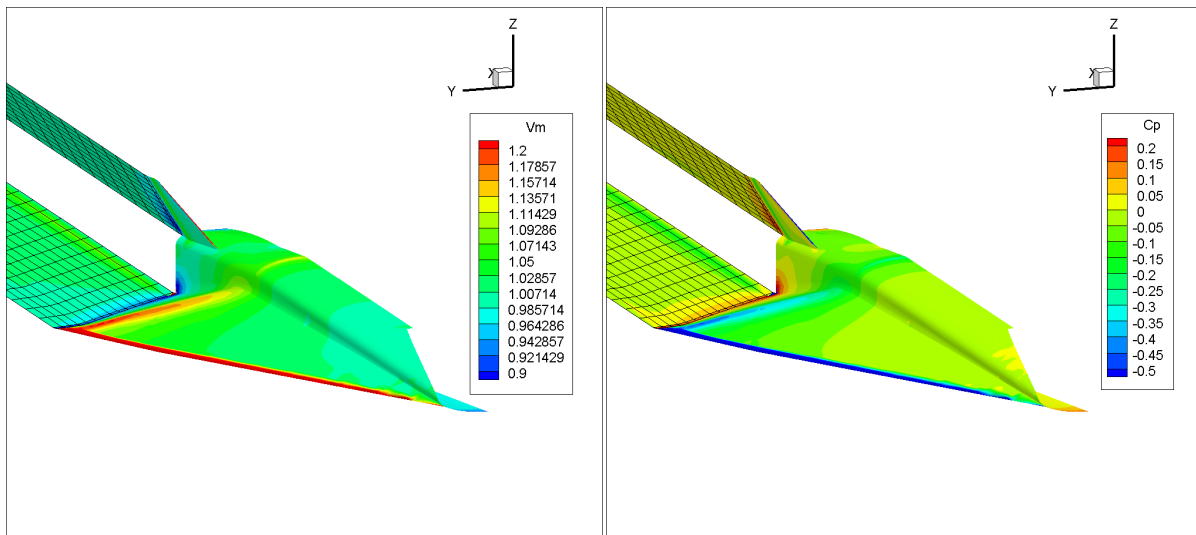


Figure 3.15: Velocity (*left*) and Pressure Coefficient (*right*) contours for $AoA = 0^\circ$, $M = 0$

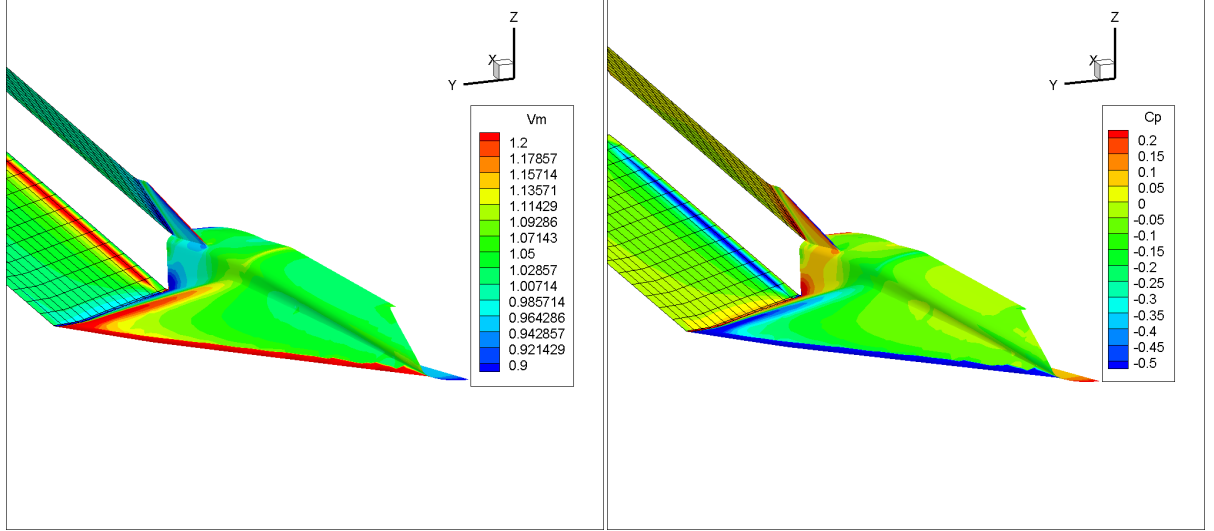


Figure 3.16: Velocity (*left*) and Pressure Coefficient (*right*) contours for $AoA=6^\circ$, $M=0$

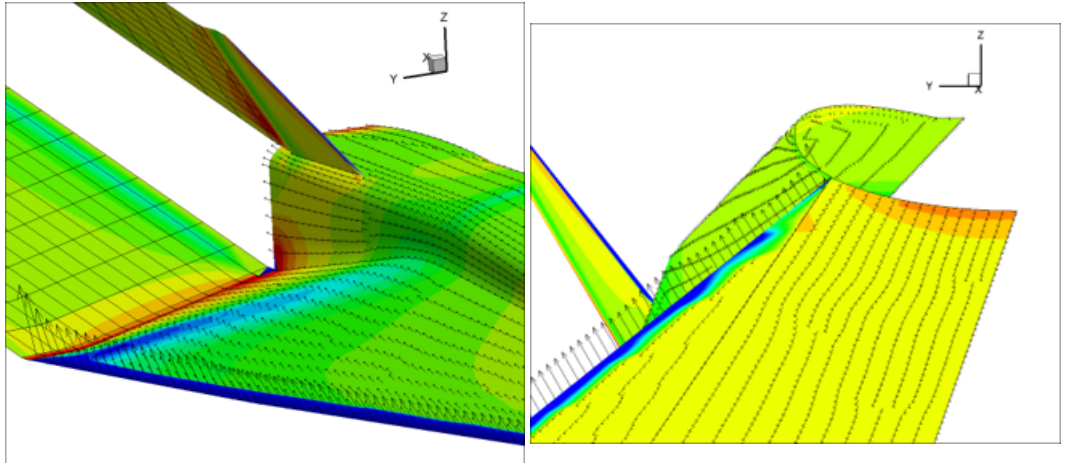


Figure 3.17: Wing upper surface detail (*left*) and Inlet stagnation area (*right*) for $AoA=0^\circ$, $M=0$

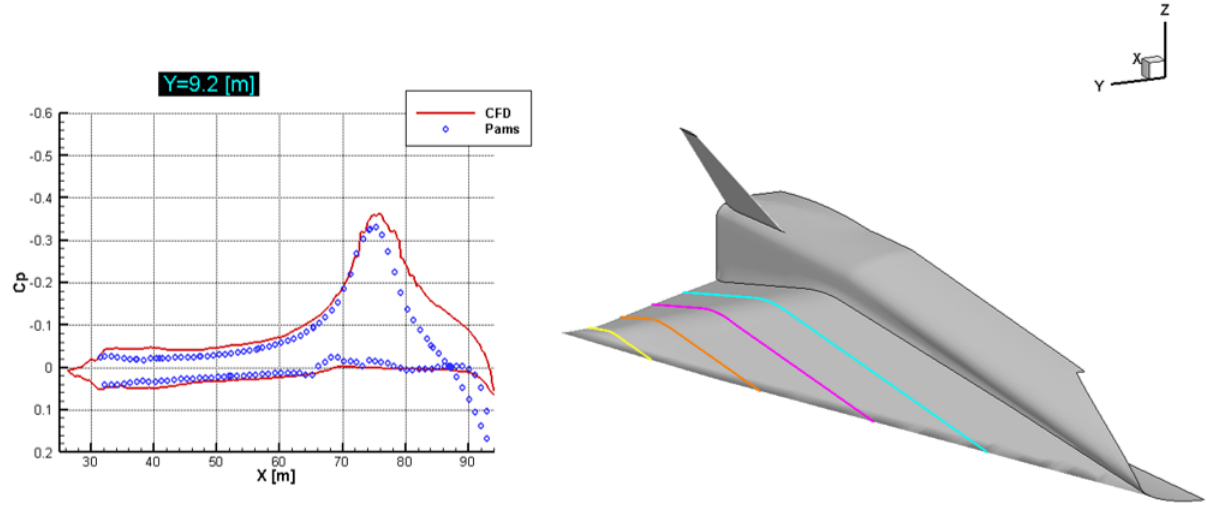


Figure 3.18: PaMS vs CFD Pressure Coefficient distribution at $y = 9.2\text{ m}$ wing section for $AoA = 0^\circ$, $M = 0.3$

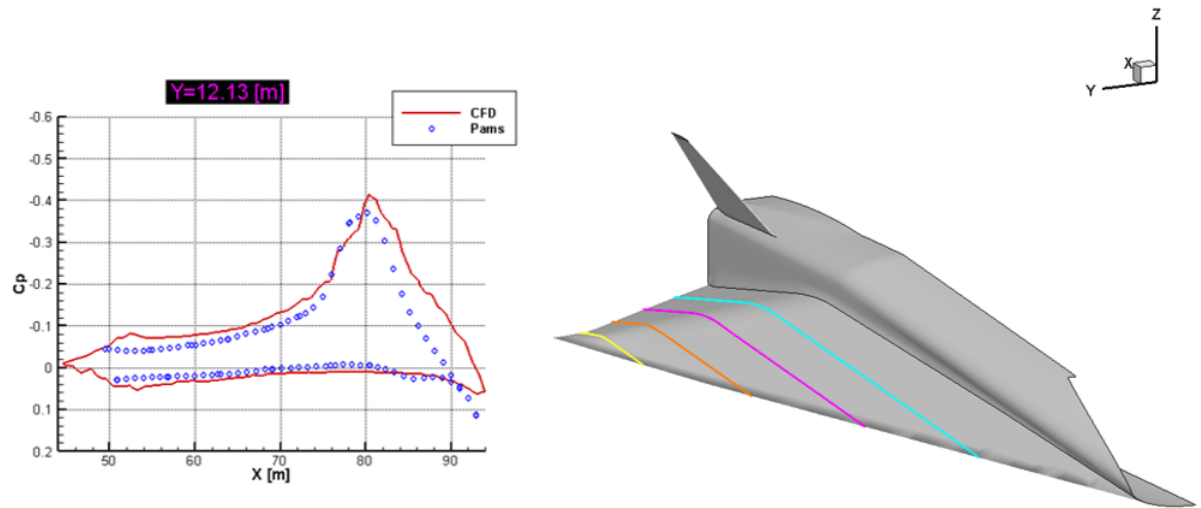


Figure 3.19: PaMS vs CFD Pressure Coefficient distribution at $y = 12.13\text{ m}$ wing section for $AoA = 0^\circ$, $M = 0.3$

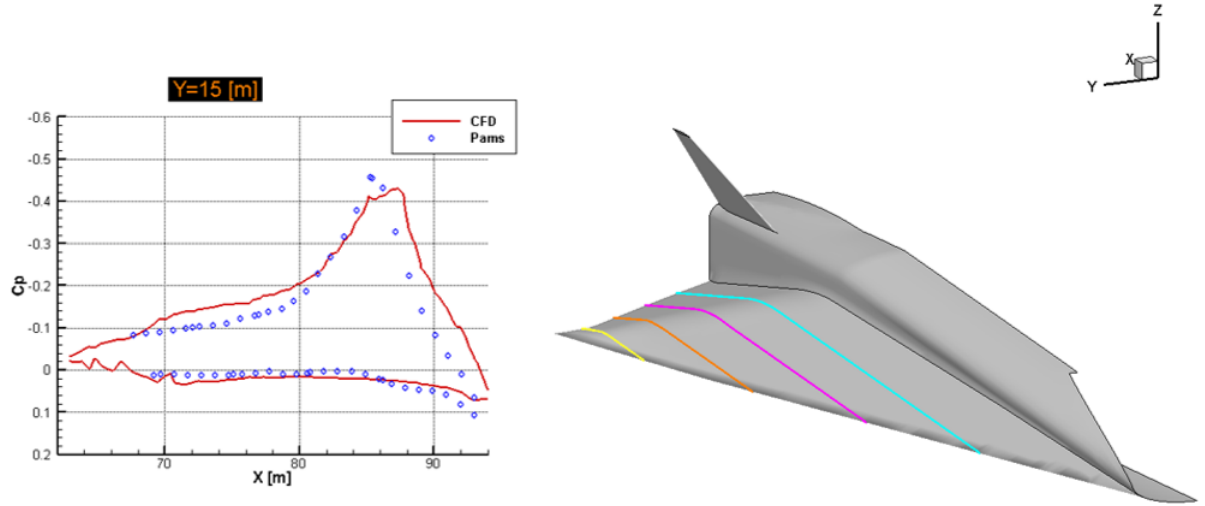


Figure 3.20: PaMS vs CFD Pressure Coefficient distribution at $y = 15$ m wing section for $AoA = 0^\circ$, $M = 0.3$

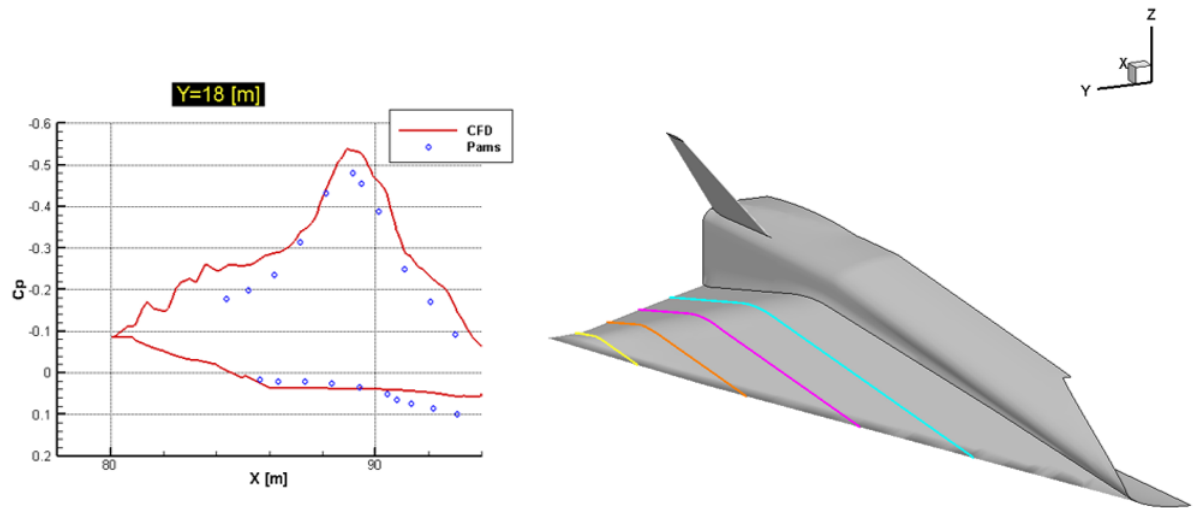


Figure 3.21: PaMS vs CFD Pressure Coefficient distribution at $y = 18$ m wing section for $AoA = 0^\circ$, $M = 0.3$

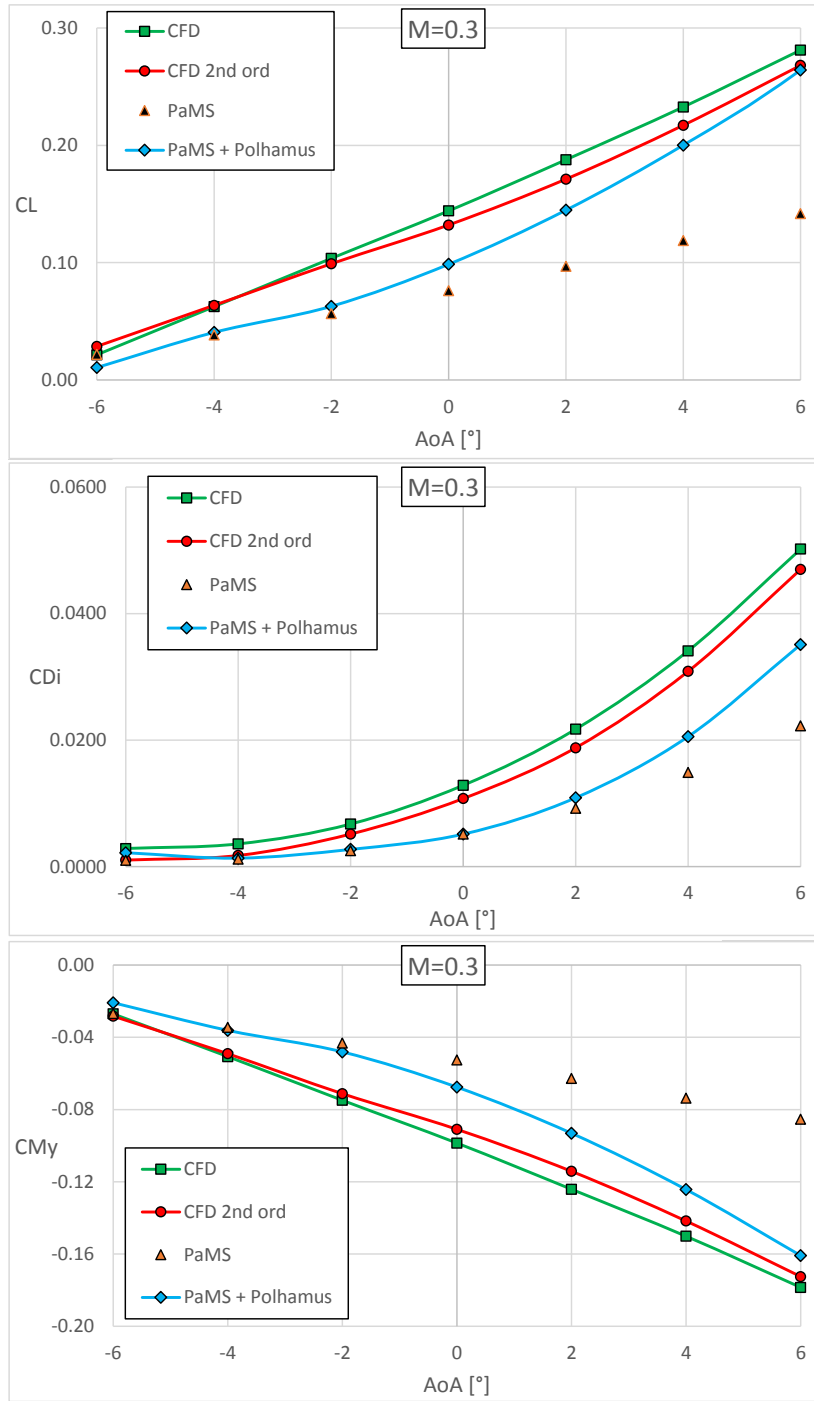


Figure 3.22: Lift (*up*), Induced Drag (*mid*) and Pitching Moment (*down*) coefficients curves for $M = 0.3$, Polhamus LE surface 10%

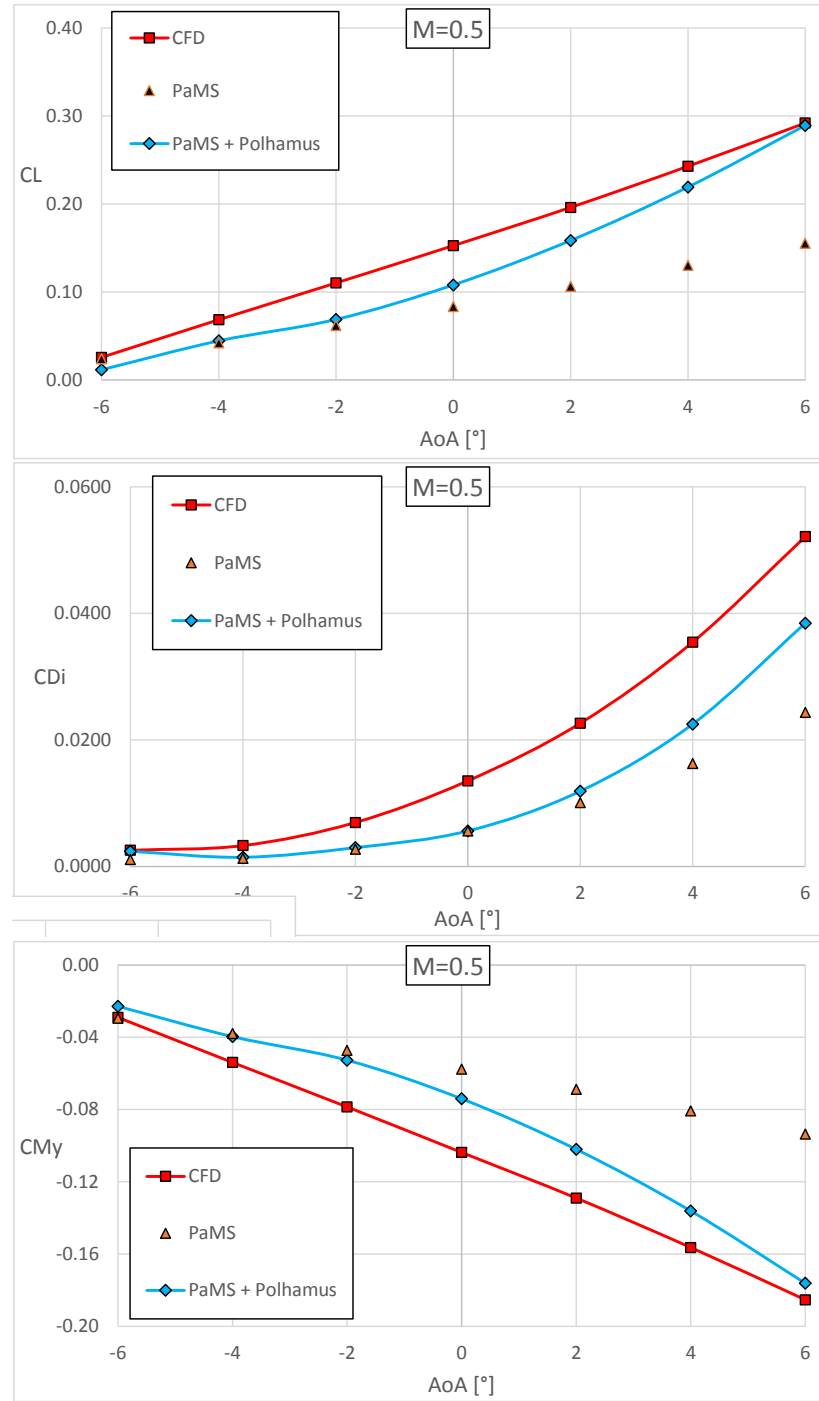


Figure 3.23: Lift (*up*), Induced Drag (*mid*) and Pitching Moment (*down*) coefficients curves for $M = 0.5$, Polhamus LE surface 10%

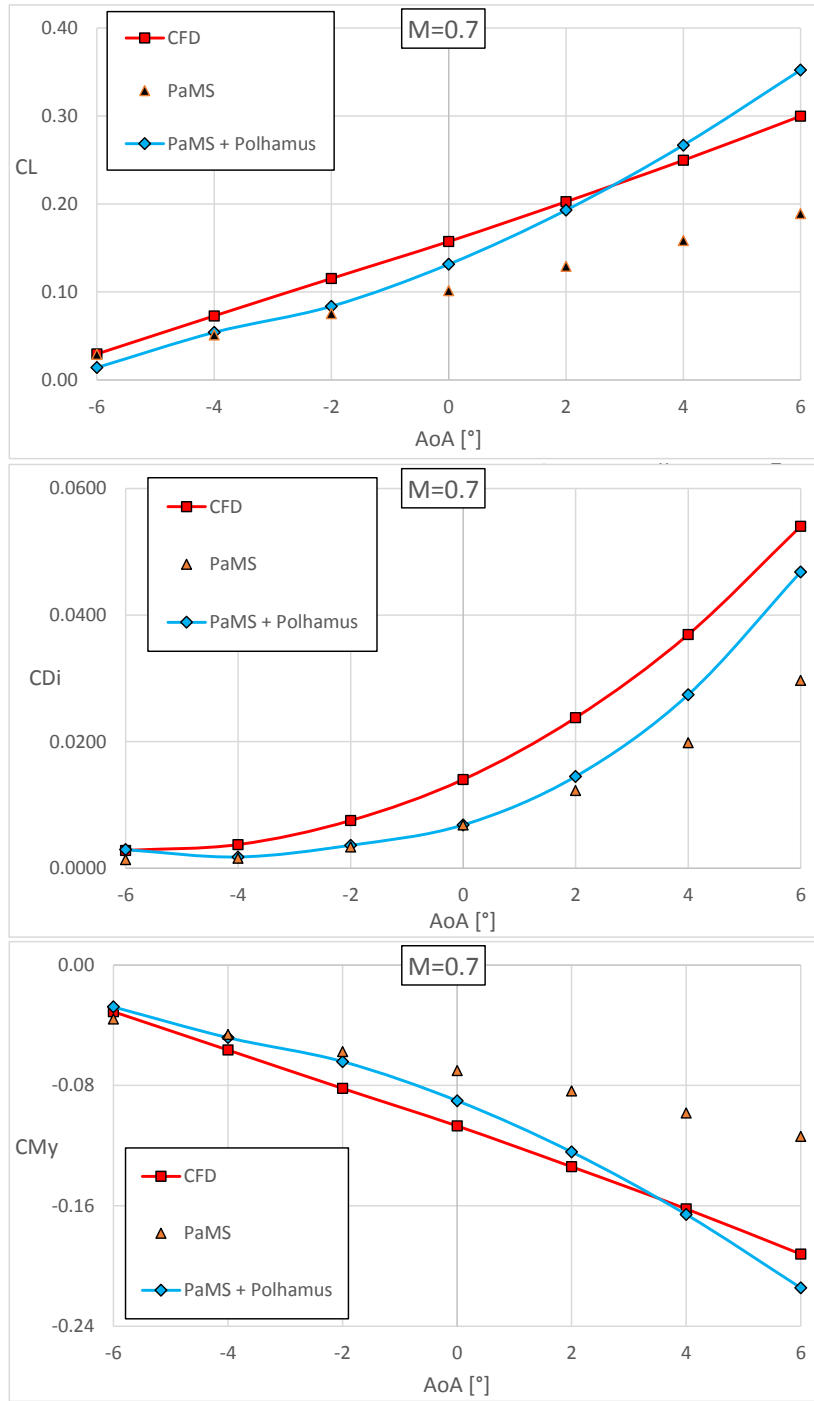
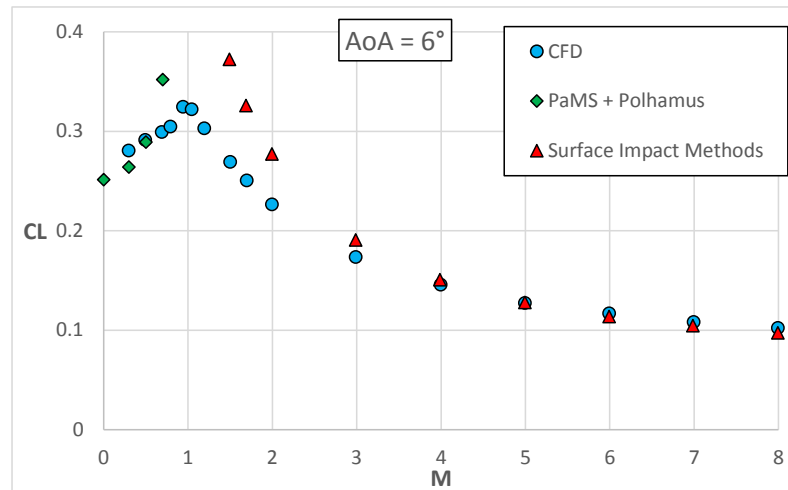
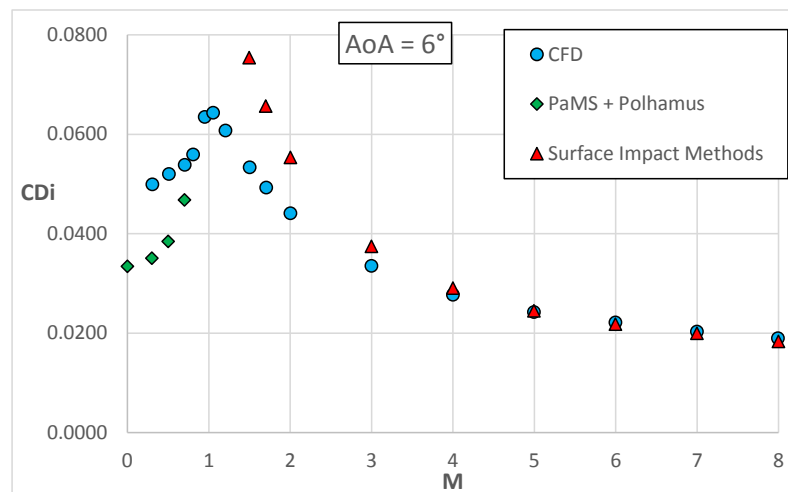


Figure 3.24: Lift (*up*), Induced Drag (*mid*) and Pitching Moment (*down*) coefficients curves for $M = 0.7$, Polhamus LE surface 10%



Lift coefficient vs Mach number for $AoA = 6^\circ$



Induced Drag coefficient vs Mach number for $AoA = 6^\circ$

Conclusions

The STRATOFly MR3 vehicle was analyzed in the range of subsonic Mach numbers using a panel method (PaMS) for ideal flows (inviscid, incompressible and irrotational). A sensitivity study of the forces in relation to the inlet captured mass flow rate was performed and an extension of PaMS capability in internal flows simulation will be investigated. Tests on the external geometry alone have been compared to CIRA Euler calculations, showing slight differences between the two approaches, due to the different resulting pressure distributions. To take into account the vortex lift contribution, Polhamus analogy was applied to the panel method solution and consequently a sensitivity study concerning the leading edge surface considered was carried out. Finally the lift, induced drag and pitching moment coefficients have been obtained, attesting PaMS capabilities in the preliminary assessment of similar design.

The selected hybrid method, based on PaMS improved by Polhamus analogy, will in conclusion be potentially useful for a further development of the aerodynamic database, including the effect of control surfaces and perhaps a lateral-directional investigation.

Bibliography

- [1] Paolo Caccavale. “*Un moderno metodo a potenziale per analisi fluidodinamiche*”.
Università degli studi di Napoli "Federico II", 2006.
- [2] Carlo de Nicola. “*Appunti per un corso di Aerodinamica degli Aeromobili*”.
Napoli, 2019.
- [3] Maskew B. “*Program VSAERO Theory Document*”.
NASA Contractor Report, 1987.
- [4] Paolo Caccavale. “*PaMS: Panel Method Solver*”. URL: http://www.fluere.it/HTML/pams_00.html.
- [5] Katz J. Plotkin A.: “*Low-Speed Aerodynamics*”.
Cambridge University Press, 2001.
- [6] Liu P.: “*A Time-Domain Panel Method for Oscillating Propulsor with both Chordwise and Spanwise Flexibility*”.
University of Canada, 1997.
- [7] Kroo I.: “*Drag Due to Lift: Concepts for Prediction and Reduction*”.
Annual Review of Fluid Mechanics Vol. 22, 2001.

- [8] Edward C. Polhamus: *“A concept of the Vortex Lift of Sharp-Edge Delta Wings based on a Leading-Edge-Suction Analogy”*.
NASA TN D3767, 1966.
- [9] J.M. Luckring: *“The discovery and prediction of vortex flow aerodynamics”*.
The Aeronautical Journal, Volume 123, 2019.
- [10] John E. Lamar Melvin H. Snyder: *“Application of the leading edge suction analogy to prediction of longitudinal load distribution and pitching moments for sharp edged delta wings”*.
NASA Langley Research Center, Technical Note, 1972.
- [11] *H2020 Stratofly Project*. URL: <https://www.h2020-stratofly.eu/>.
- [12] P. Roncioni M. Marini G. Saccone R. Fusaro N. Viola: *“Preliminary Numerical Characterization of STRATOFly Vehicle’s Intake”*.
International Conference on Flight Vehicles, Aerothermodynamics, Re-entry Missions, and Engineering (FAR), 2019.
- [13] T. Langener S. Erb J. Steelant: *“Trajectory Simulation and Optimization of the LAPCAT-MR2 Hypersonic Cruiser Concept”*.
29th Congress of the International Council of the Aeronautical Sciences, 2014.
- [14] J. Steelant R. Varvill S. Defoort K. Hannemann M. Marini: *“Achievements Obtained for Sustained Hypersonic Flight within the LAPCAT-II project”*.
20th International Space Planes, Hypersonic Systems, and Technologies Conferences, 2015.

- [15] M. Marini S. Hernandez B.H. Saracoglu A.C. Ispir K. Lammers P. Natale L. Cutrone P. Roncioni R. Fusaro N. Viola: *“STRATOFly Project Challenges in the Fields of Airframe, Aerothermodynamics, High-Speed Propulsion and Energy Management System”*. International Conference on Flight Vehicles, Aerothermodynamics, Re-entry Missions, and Engineering (FAR), 2019.

*Dopo più di due anni mi ritrovo nuovamente qui,
a riservare i miei pensieri
alle persone cui più devo il raggiungimento di questo traguardo...
la mia fortuna più grande è che tali persone siano ancora le stesse, rimaste
costantemente al mio fianco.*

*Ringrazio poi la straordinaria squadra che mi ha permesso di realizzare
questo lavoro. Ringrazio specialmente l'avermi fatto sentire sempre sullo
stesso gradino.*

*Il Dott. Roncioni ed il Dott. Schettino, sempre presenti nonostante le
distanze. Il Dott. Caccavale, di cui ringrazio l'instancabile professionalità,
pazienza e curiosità.*

*In ultimo, ma non per importanza, desidero sinceramente ringraziare il
Prof. de Nicola, di cui conserverò la saggezza, le risate
ed ancor di più le bastonate...*